Eidgenössische Technische Hochschule Zürich
Swiss Federal Institute of Technology Zurich

Nonclassical Light in waveguide QED: Amplitude and Intensity Correlations

Master Thesis

Bradley K. Mitchell

May 18,2016

Advisors: Dr. Simone Gasparinetti, Prof. Dr. Andreas Wallraff

Department of Physics, ETH Zürich

Abstract

Waveguide quantum electrodynamics (QED) explores interactions between atoms and light at the quantum level in one-dimensional open space. In particular, the experimental platform of superconducting circuits enables strong interactions between "artificial atoms" and a one-dimensional electromagnetic continuum of modes. A powerful tool for measuring such interactions, employed extensively in circuit QED, is the measurement of intensity correlation functions with linear detection. In this thesis, I have measured amplitude and intensity correlations of microwave light emitted by an artificial atom in 1-D open space, probing both its fundamental and higher transitions. This was done using a quantum signal analyzer developed at Qudev, consisting of fast FPGA electronics and a nearly quantum-limited, phase-insensitive linear amplifier. I discuss how noise influences the measured field correlations, considering both thermal noise that acts on the artificial atom, and noise that is added during measurement. Understanding these noise sources in the experiment is key to choosing the signal-processing steps and experimental methods appropriate for measuring nonclassical light statistics in the waveguide QED platform. The results herein provide guidance toward the measurement of photon correlations in the waveguide QED platform. This capability would advance the study of quantum optical phenomena in 1-D open space, such as interaction of itinerant photons via atoms and long-distance entanglement between multiple atoms.

Contents

List of Figures

Chapter 1

Introduction

1.1 Motivations of waveguide quantum electrodynamics

The study of light and matter at fundamental levels offers potential for both technological advance and insight into nature. In particular, engineering interactions of single atoms with individual photons provides the precision to understand and harness the two media at the most fundamental level. Such precise study leads to deeper understanding of quantum mechanics and quantum electrodynamics, as well as development of devices which take advantage of unique interactions only achievable in such systems.

To study a single atom interacting with a single photon at first seemed daunting. The dipole moment $\vec{d}$ of a single atom is quite small, owing to the mean charge-separation of electrons in atoms being small, and the field strength $\vec{E}_0$ of a laser at the single-photon level is also very weak, making the interaction energy $\vec{d} \cdot \vec{E}_0$ very small. This small interaction energy meant that no quantum coherence at the single photon level was observable between a photon and an atom. The breakthrough was when the field of cavity quantum electrodynamics (cavity-QED), which studies the interaction of atoms with laser light trapped in an optical cavity, first achieved strong coupling between laser light and a single atom; that is, the frequency of interaction between the atom and a single photon in the field is larger than the coupling of the environment to the field or the atom respectively, heralded by the observation of vacuum Rabin splitting in 1992 [39]. By using photons trapped in a cavity, the number of interactions the atom has with the single photon was strongly enhanced, overcoming the small interaction energies of propagating light with single atoms.

With the invention of solid-state superconducting "artificial atoms" [32] came the study of circuit QED; the artificial atoms in this platform interact with coherent microwave tones in a microwave transmission line, instead of a laser, and these systems can be fabricated with industry-standard microwave circuit fabrication technologies. In 2004, vacuum Rabi splitting of an artificial atom and the fundamental mode of a microwave superconducting coplanar-

waveguide resonator, was achieved [43], which heralded the study of "quantum optics on a chip". The advantages of circuit QED that make it so amenable for studying coherent interactions between atoms and fields are that the mode volume the microwave field is extremely small, resulting in electric fields in the coplanar waveguide resonators $E_{\mathrm{rms}} \approx 0.2\,\mathrm{V\,m^{-1}}$, and the large effective dipole moment of the artificial atoms, which, unlike real atoms, can be engineered. This platform thus circumvents the small field-atom coupling which, before cavity QED, limited strong light-matter interaction experiments with conventional atoms and laser light.

With these accomplishments, the study of quantum optics can extend beyond cavity QED. Specifically, one would like to explore the interaction of atoms with *itinerant*, or propagating, light fields. For instance, the study of how atoms interact via long- or medium-range photonic exchange and how flying photons effectively interact when in the presence of atoms are questions which can be studied with an "open-space" experimental platform. The seemingly natural choice of studying this via natural atoms and optical light suffers from poor overlap between a propagating light field and the radiation pattern of an atom in free space, in addition to the small dipole coupling described. That is, the field amplitude scales$\sim r^{-2}$ in distance r from the atom, making the study of long-range photon-mediated interactions of atoms in 3-D space difficult. This of course was not an issue in a cavity, where the density of optical states to which the atom could emit are restricted by the boundary conditions of the cavity.

The circuit QED platform, however, does not suffer from these shortcomings. As an experimental platform which reduces the dimensionality of both atoms and the electromagnetic spectrum of open space to effectively one dimension, circuit QED maintains the strong coupling between "artificial atoms" and 1-D open space due to the mode geometry, unchanged between the cavity and "free-space" cases, of the microwave light and the virtually unit overlap between atomic emission and the itinerant microwave modes of the coplanar waveguide. Secondly, the geometry of 1-D space means that emitted radiation does not reduce in energy density with distance, as the energy is not distributed over any solid angle. In some sense, the cavity mode is "0-D", in that it is confined by all dimensions for both optical and superconducting realizations, while the itinerant mode in a coplanar waveguide is "1-D", as opposed to the itinerant optical mode, which allows atomic emissions into 3-D, unconfined space.

The design features of 1-D quantum optical systems have produced great insights into fundamental questions about interactions of single atoms and single photons. Initial experiments measured resonance fluorescence of a single artificial atom, and the near-unit extinction of light by the atom at single-photon powers [3], followed by time-resolved dynamics [2] and electromagnetically induced transparency [1]. The second-order correlation function of a single artificial atom in open 1-D space has also been measured [20], as well as the implementation of a single-photon router [21].

The Quantum Device Lab (Qudev) has since extended the waveguide QED platform by measuring resonance fluorescence of coupled artificial atoms, which, depending on the number of emission wavelengths they were separated by in the waveguide, formed sub- and super-radiant states [41]. Substantial theoretical work has also investigated field correlations resulting from several interacting atoms aligned together in a waveguide [25]. These systems could potentially shed light on the generation of photon-photon interactions and entanglement generation, mediated via atoms in a waveguide [44].

The current goal of the waveguide QED project at Qudev is to measure second-order correlations of the microwave light emitted by two artificial atoms in 1-D open space. The technology to perform such measurements in microwave systems has been pioneered by experiments demonstrating photon-blockade [26] and Hong-Ou-Mandel interference [27]. Integrating the correlation measurements with the waveguide-based systems would propel the study of many atoms interacting via a continuum of modes in one-dimensional quantum optics.

1.2 Planar superconducting transmission lines

The primary structure used in superconducting circuit technologies is the coplanar waveguide (CPW). It is the two-dimensional analog of a coaxial cable, consisting of a central "signal" line with two ground planes, connected by air-bridges, surrounding it. As this structure has two electrically distinct conductors, it can support transverse electric- and magnetic-field (TEM) modes with no cutoff frequency. This is what distinguishes the transmission line from any general waveguide. This transmission line can be described as a chain of capacitances and inductances, as shown in figure 1.1. The capacitance c and inductance l per unit length Δx define the characteristic impedance $Z = \sqrt{\frac{l}{c}}$ of the waveguide, as well as the speed of light $v = 1/\sqrt{lc}$. This is seen easily by the Telegrapher's equations [35]

$$\begin{aligned} \partial_x V &= -l\partial_t I \\ \partial_x I &= -c\partial_t V \end{aligned} \tag{1.1}$$

Combining these into one equation for the voltage V, we get the wave equation for the system

$$\partial_{xx} V = \frac{1}{lc}\partial_{tt} V \tag{1.2}$$

Just as in the coaxial cable, the TEM mode for the CPW has the electric field between the central line and the surrounding ground plane, with the magnetic field encircling the center line. By applying the canonical techniques of quantizing the Lagrangian for the field, derived from the Telegrapher's equations, these structures constitute a bosonic continuum in one dimension for the microwave field, a fundamental geometry for the study of the interactions between light and matter at the quantum level. To reach the quantum level,

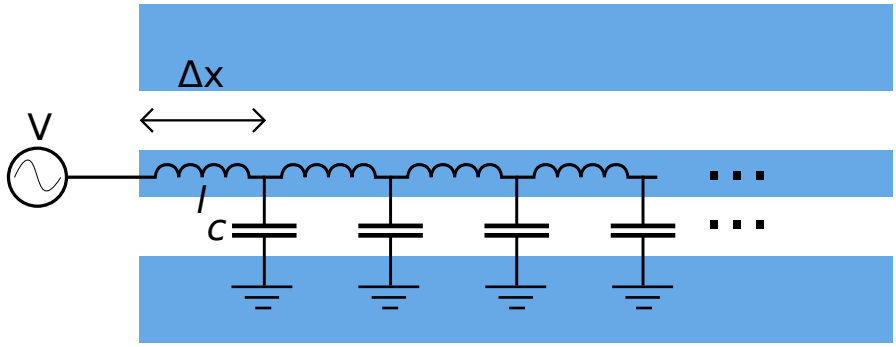

Figure 1.1: A depiction of the geometry and lumped-element schematic of a coplanar waveguide.

however, the devices need to be low-loss, as dissipation destroys coherence of quantum states by continuous measurement by the environment on the system. Therefore, the devices are fabricated out of superconducting materials, typically Nb or Al, which have nominal critical temperatures T_c of 9.8 K and 1.2 K, respectively.

1.3 The transmon artificial atom

An artificial atom is simply a quantum system with an engineered energy spectrum such that transitions are individually addressable. This is not the case for resonators, because their energy spectrum is harmonic and therefore the energy is linear in the number of of energy quanta. The invention that eventually heralded the field of superconducting quantum information processing is the the nonlinear, virtually dissipationless circuit element, the Josephson tunnel junction.

1.3.1 The Josephson junction: a nonlinear circuit element

The Josephson junction consists of two superconducting regions separated by a non-superconducting element. For example, $Al - Al_2O_3 - Al$ is a S-I-S (superconductor-insulator-superconductor) type of Josephson junction, commonly used for all quantum devices discussed in this thesis. In 1962 [22], Brian Josephson predicted current-phase relationship for such junctions, now called the Josephson effect. The Josephson relations

$$I_s = I_c \sin\phi \tag{1.3}$$

$$\frac{d\phi}{dt} = \frac{2eV}{\hbar} \tag{1.4}$$

describe how the current across the junction is periodic in the phase-difference ϕ of the superconducting order parameter on either side of the junction [40].The phase changes with the voltage, scaled by the $2e$, the charge of the superconducting carrier, the Cooper pair, and $\hbar$. The critical current I_c is material- and temperature-dependent. From these relationships, one can invoke Faraday's

law to obtain the inductance

$$\begin{aligned} L(\phi) \equiv \frac{V}{\dot{I}} &= \frac{\hbar}{2eI_c}\frac{\dot{\phi}}{\cos\phi\,\dot{\phi}} \\ &= \frac{\Phi_0}{2\pi I_c \cos\phi} \\ &= \frac{L_{J0}}{\cos\phi}, \end{aligned} \tag{1.5}$$

where $\Phi_0 = h/2e$ is the flux quantum and $L_{J0} = \frac{\Phi_0}{2\pi I_c}$ is the Josephson inductance. Thus, the Josephson relations in (1.3) gives an inductor whose inductance depends on the flux threading the junction, once more by Faraday's law. Though ϕ is the phase of the superconducting wavefunction, the gauge-invariance of the Schrödinger equation in a vector potential $\boldsymbol{A}$ relates magnetic flux to wave function phase, and through flux quantization of a superconducting loop, the phase threading the junction is then quantized [40]. Appendix A.1 gives some more detail on this point.

In the following section, I will outline the circuit design of the transmon artificial atom, a variant of this nonlinear oscillator I've described here, and describe the spectrum under appropriate approximations.

1.3.2 Design of the transmon

The basic design of the transmon artificial atom [23], shown in figure 1.2, is to place two Josephson junctions (symbolized by the crossed boxes) in parallel, forming a superconducting quantum interference device, or SQuID. It can be shown that this has the same current relationship as a standard Josephson junction, except with a critical current $I_c(\Phi)$(see appendix A.1) [42] which is tunable with externally applied magnetic flux Φ. This tunability enables us to adjust the resonant frequency, and therefore the interactions of transmons with each other and with resonators in situ.

The energy spectrum of the transmon is dominated by the Josephson energy $E_J(\Phi)$ as compared to the charging energy E_C, with

$$E_J(\Phi) = \frac{\Phi_0}{2\pi} I_c(\Phi) \tag{1.6}$$

$$E_C = \frac{e^2}{2C_\Sigma}, \tag{1.7}$$

where $C_\Sigma = C_B + C_J$ is the total capacitance of the system, including both the designed capacitance C_B in figure 1.2 and the small capacitance of the junctions C_J. The Hamiltonian can be written in terms of the number of charges on the charge island N and the phase across the SQuID loop ϕ, and this is known as the Cooper-pair box Hamiltonian [5]:

$$H_{CPB} = 4E_C\left(N - N_g\right)^2 - E_J(\Phi)\cos(\phi) \tag{1.8}$$

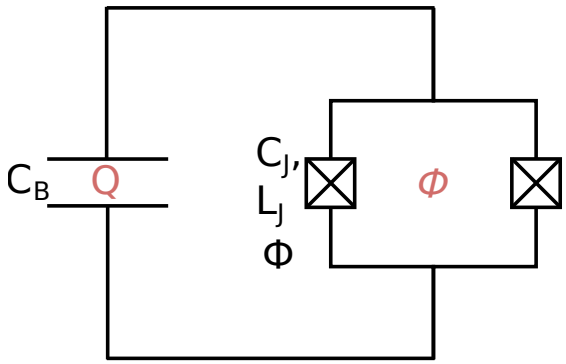

Figure 1.2: Circuit diagram for the transmon artificial atom. Red letters Q and ϕ denote the atomic canonical operators of the circuit. The junctions have small shunt capacitance C_J, and nonlinear inductance L_J, tunable by an applied magnetic flux Φ. This in conjunction with a larger shunt capacitor C_B forms a nonlinear LC resonator.

This is obtained simply by relating $Q^2 = (2e(N - N_g))^2$, where we've assumed there is a gate charge that supplies charges to the island in figure 1.2, and As described in detail in [23], applying perturbation theory around $\Phi = 0$ in the limit of $(E_C/E_J)^{-1} \ll 1$, the Hamiltonian for the transmon can be approximated as a Duffing oscillator, giving a spectrum

$$E_m \simeq -E_J + \sqrt{8E_C E_J}\left(m + \frac{1}{2}\right) - \frac{E_C}{12}\left(6m^2 + 6m + 3\right) \tag{1.9}$$

Thus, the anharmonicity $\alpha \equiv E_1 - E_0 \simeq -E_C$ in the limit of large E_J/E_C. The frequency $\omega_p \equiv \sqrt{8E_C E_J}/\hbar$ is the Josephson plasma frequency; hence the name "transmon", meaning transmission-line shunted plasma oscillation qubit [23].

1.3.3 Coupling the transmon to a waveguide

As discussed in section 1.2, the coplanar waveguide is an attractive method to realize a 1-D bosonic continuum, enabling strong mode-matching to other planar structures. That is, the transmon coupled to a coplanar waveguide enables the study of quantum optics with a continuum of modes with strong coupling, unlike real atoms interacting with a laser, due to their poor mode-matching. Indeed, this work builds on those in [3, 41, 20], and others, with the works mentioned having observed phenomena like near-unit reflection of light by a single artificial atom, inter-atom-coupling via the waveguide, and photon anti- and super-bunching respectively.

To accomplish this, the atom is coupled capacitively to the waveguide, as shown in the circuit schematic in figure 1.3. The two capacitances C_{g1} and C_{g2} form an effective coupling capacitance C_g (see [23]). Via this capacitive coupling, the artificial atom is coupled via its large dipole moment to the 1-D bosonic continuum of states present in the waveguide.

The next chapter. details the theoretical description of light-matter interaction waveguide QED, specifically relevant to the experiments presented in the following chapters.

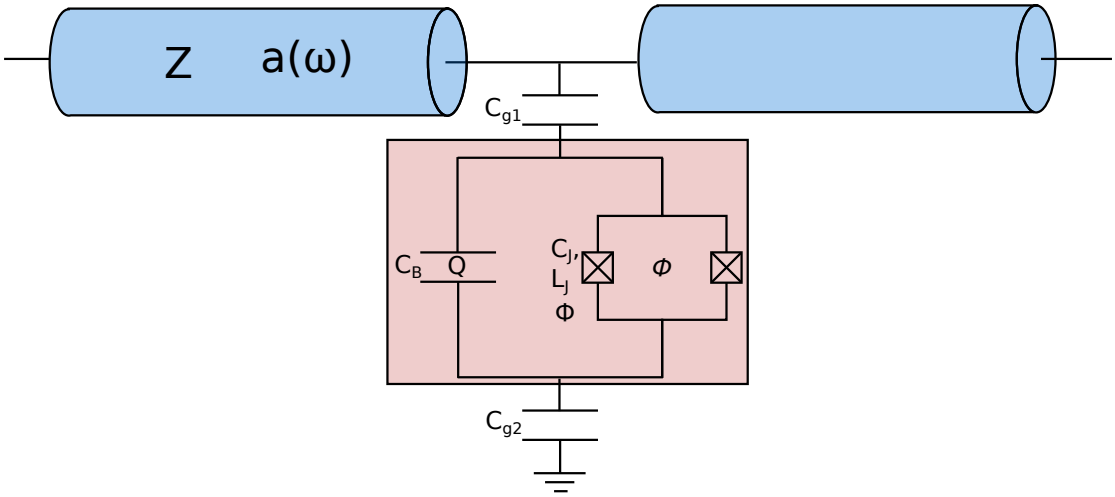

Figure 1.3: Circuit schematic of a transmon with canonical operators Q and Φ coupled by capacitance C_{g1}, C_{g2} to the center line and ground of a waveguide with characteristic impedance Z and bosonic field $a(\omega)$

1

Chapter 2

Theory of nonclassical light in wQED

In this chapter, I discuss the central theory for the interaction of a single transmon with the microwave field in a waveguide, including both two-level and three-level dynamics. Furthermore, I discuss how to predict measurable quantities like transmittance, amplitude, and photon correlations. Much of the theory in this section is adapted from Lalumière et al. [25], simplified to our experiments.

2.1 Master equation for a qubit in a waveguide

2.1.1 Two-level dynamics

The Hamiltonian contains three primary terms: the energy of the field H_F, the atom H_A, and their interaction H_I. These are written as [25]

$$H_F = \int_0^\infty \mathrm{d}\omega\, \hbar\omega \left[a_{\mathrm{R}}^\dagger(\omega) a_{\mathrm{R}}(\omega) + a_{\mathrm{L}}^\dagger(\omega) a_{\mathrm{L}}(\omega) \right] \tag{2.1}$$

$$H_A = \hbar\omega_A \sigma_z / 2 \tag{2.2}$$

$$H_I = \hbar g \left(\Xi + \Xi^\dagger \right) \sigma_x \tag{2.3}$$

Conceptually, equation (2.1) describes the creation of left- and right-propagating photons in a continuum of one-dimensional modes a_{L} and a_{R}, respectively. The atom Hamiltonian H_A is an abstract two-level system with energy $\hbar\omega_A$, with $\sigma_z \equiv |e\rangle\langle e| - |g\rangle\langle g|$, and the interaction term couples the atom transversally, obtained traditionally by considering dipole coupling g of the atom to the field by the atom's state-transition operator $\sigma_x = |e\rangle\langle g| + |g\rangle\langle e|$ and the field operator Ξ given by [25]

$$\Xi = -i \int_0^\infty \mathrm{d}\omega\, \sqrt{\omega} \left[a_L(\omega) e^{-i\omega x_A / v} + a_R(\omega) e^{i\omega x_A / v} \right] \tag{2.4}$$

This is related to the electric field at the location of the atom x_A. By solving Heisenberg's equation of motion for mode $a(\omega, t)$ of the waveguide, one

can re-express the field operator Ξ in terms of the input state and a term dependent on the coupling to the atom. After making the Markov, long-time, and rotating-wave approximations, absorbing Lamb shifts into the atomic energies, and ignoring small non-positive terms in the field operator Ξ (see [25]), the master equation for the density matrix ρ of the atom of the form

$$\dot{\rho} = -\frac{i}{\hbar}[H, \rho] + \Gamma\left[\sigma_- \rho \sigma_+ - \frac{1}{2}\{\sigma_+\sigma_-, \rho\}\right] \tag{2.5}$$

is obtained, with Γ as the decay rate of the atom into the field, and $\sigma_- = |g\rangle\langle e| = \sigma_+^\dagger$ is the atomic lowering operator. Though not the original, further information of the theory behind this thesis can be obtained in [25]. The effective Hamiltonian for the atom in equation (2.5) is

$$H = H_A + \hbar d(t)\sigma_x \tag{2.6}$$

with $d(t)$ corresponding to the field Ξ driving the system. Assuming the qubit is driven from the left at power P with frequency ω_d,

$$d(t) = 2\sqrt{\frac{\Gamma}{2}}\left(\sqrt{\frac{P}{\hbar\omega_A}}\sin(\omega_d t)\right) \tag{2.7}$$

The dynamics of the system are invariant under unitary transformations because unitary transformations are merely a change of basis, and physical theories must be invariant under basis transformations. Moving into the rotating frame by transforming the dynamics into the frame of the drive with $U(t) = \exp\left(-i\omega_d b^\dagger b t/2\right)$, where here b denotes the lowering operator for the transmon, is one such transformation. By transforming the Hamiltonian into this time-dependent rotating frame basis (see appendix A.2) and making the rotating wave approximation (thereby discarding fast-rotating terms in the rotating frame, for they average to zero), the Hamiltonian in the rotating frame reads

$$H = \hbar\frac{\delta\omega}{2}\sigma_z + \hbar\frac{\Omega}{2}\sigma_x \tag{2.8}$$

$$= \hbar\begin{pmatrix} -\frac{\delta\omega}{2} & \frac{\Omega}{2} \\ \frac{\Omega}{2} & \frac{\delta\omega}{2} \end{pmatrix} \tag{2.9}$$

or, in the undriven atomic basis $\{|g\rangle, |e\rangle\} = \{(1\,0)^T, (0\,1)^T\}$, where $(\cdot)^T$ denotes the transpose and $\delta\omega = \omega_A - \omega_d$ is the detuning of the transition from the drive tone. Because we are in the frame of the drive, the drive $d(t)$ is no longer time-dependent (in the rotating-wave approximation), and so we define the Rabi rate of the system

$$\Omega = 2\sqrt{\frac{\Gamma}{2}}\sqrt{\frac{P}{\hbar\omega_A}}, \tag{2.10}$$

which is the amplitude of the applied coherent state constituting the "laser" drive. Using Fermi's golden rule, in the approximation that the initial state

is the qubit excited state $|e\rangle$ and the final state is the ground state $|g\rangle$, the radiative decay rate of the qubit in the frame of the qubit is

$$\Gamma = 4\pi g^2 \omega_A \tag{2.11}$$

The (dimensionless) coupling coefficient g of the atom to the field is given in terms of transmon parameters is derived in [25]. This can be expressed in terms of the transmission line impedance Z, the resistance quantum R_K, the capacitance between the waveguide and transmon C_g, and the total capacitance of the transmon C_Σ as

$$g = \sqrt{\frac{Z}{R_K}} \frac{C_g}{C_\Sigma} \left(\frac{E_J}{8E_C} \right)^{\frac{1}{4}}. \tag{2.12}$$

With these relations, one may then substitute equation (2.8) into the master equation 2.5 to determine the dynamics of the two-level system. The system of linear equations solving the expectation values of the elements of ρ are called the optical Bloch equations [7]. These equations are quite general, describing quasi-resonant driving of a transmon transition by an externally applied coherent field. The uniqueness to wQED comes from the fact that only two 1-D modes are involved in the interaction Hamiltonian, which is seen in the ratios of the coupling to the driving field and the total radiative decay rate. The next section discusses the case for when three levels of the transmon are considered.

2.1.2 Three-level dynamics

To obtain an effective Hamiltonian for the transmon with three levels, we simply include the third excitation for the solution to the transmon Hamiltonian as given in 1.3.2, whose eigenstates have frequencies ω_{ge} for the $|g\rangle \rightarrow |e\rangle$ transition, and $\omega_{ef} = \omega_{ge} + \alpha$ for the $|e\rangle \rightarrow |f\rangle$ transition, where $\alpha \simeq E_C$ [23] is the anharmonicity of the transmon. So the atomic Hamiltonian is of the form

$$H_A = \frac{\hbar}{2}\omega_{ge}\sigma_z^{(0)} + \frac{\hbar}{2}\omega_{ef}\sigma_z^{(1)} \tag{2.13}$$

with $\sigma_z^{(0)} = |e\rangle\langle e| - |g\rangle\langle g|$ and $\sigma_z^{(1)} = |f\rangle\langle f| - |e\rangle\langle e|$. Generally, $\sigma_z^{(n)} = |n+1\rangle\langle n+1| - |n\rangle\langle n|$. That is, H_A is a ladder Hamiltonian, where states $|g\rangle$ and $|f\rangle$ are not coupled directly. One can use the general formalism outlined in [25] to extend this from the two-level dynamics to three. Crucially, the damping rate of the transitions to the field depend on the level of the transition, modifying equation 2.11 as

$$\Gamma_n = 4\pi g^2 (n+1)\omega_{(n+1,n)} \tag{2.14}$$

In this notation, $\omega_{ge} = \omega_{(1,0)}$, and so on. Note that in this thesis, $\Gamma \equiv \Gamma_0$ refers to the damping of the fundamental mode. The Rabi rate for each level $\Omega_n = \sqrt{n+1}$, where $\Omega_0 = 2\sqrt{2\pi g^2 P/\hbar}$. The effective Hamiltonian for the driven three-level artificial atom is then, in the rotating frame of the drive

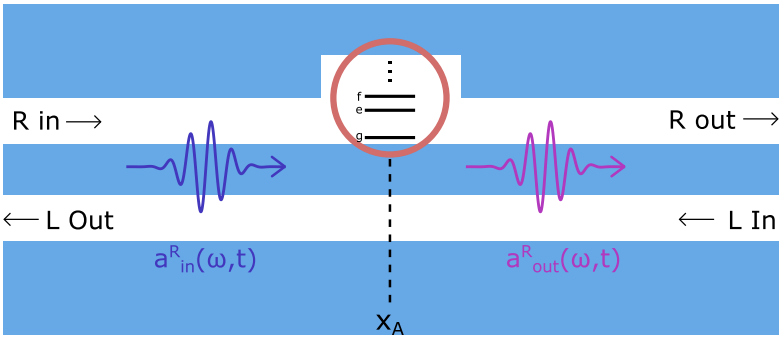

Figure 2.1: Input-output theory schematic in wQED. The input field (purple) travels down the waveguide (blue), interacts with the quantum system (red circle) at location x_A, and the output produced a_{out} is a combination of input light and nonclassical light from the quantum system.

frequency ω_d

$$H = \frac{\hbar}{2}\left(\omega_{ge} - \omega_d\right)\sigma_z^{(0)} + \frac{\hbar}{2}\left(\omega_{ef} - \omega_d\right)\sigma_z^{(1)} + \hbar\frac{\Omega_0}{2}\sigma_x^{(0)} + \hbar\frac{\sqrt{2}\Omega_0}{2}\sigma_x^{(1)} \tag{2.15}$$

Here $\sigma_x^{(n)} \equiv \sigma_+^{(n)} + \sigma_-^{(n)} = |n+1\rangle\langle n| + |n\rangle\langle n+1|$ is the transversal population exchange between transmon level $|n+1\rangle$ to $|n\rangle$ and Γ_n is expressed in terms of Γ_0 as $\Gamma_n = (n+1)\Gamma_0\omega_{(2,1)}/\omega_{(1,0)}$. In matrix form with $|g\rangle \to (1\,0\,0)^{\mathrm{T}}$, $|e\rangle \to (0\,1\,0)^{\mathrm{T}}$, and $|f\rangle \to (0\,0\,1)^{\mathrm{T}}$, we then have

$$H = \hbar\begin{pmatrix} 0 & \Omega_0/2 & 0 \\ \Omega_0/2 & \left(\omega_{ge} - \omega_d\right)/2 & \sqrt{2}\Omega_0/2 \\ 0 & \sqrt{2}\Omega_0/2 & \left(\omega_{ge} + \omega_{ef} - \omega_d\right)/2 \end{pmatrix} \tag{2.16}$$

2.2 Input-output theory

Input-output theory describes how to predict the statistics of the light of the output field coupled to atom, given the input field and the Hamiltonian describing the time-evolution of the waveguide modes $a^{(L,R)}(\omega,t)$. This tool is used both for transmittance and reflectance, as well as two- and four-time correlations. For simplicity, we consider the input state to be $a_{\text{in}}^R(\omega,t)$, moving toward the right, and one output state a_{out}^R; the other combinations of inputs and outputs for left- and right-moving modes generalize easily. Clearly, if the light input does not interact with anything, then $a_{\text{out}}^R(\omega,t) = a_{\text{in}}^R(\omega,t)$. But if the waveguide is non-empty, then the interaction Hamiltonian H_I will determine the Heisenberg equation of motion for the output mode; that is, after the light has interacted with the quantum system. This is analogous to what was stated in section 2.1.1 to determine the solution of the field operator Ξ before getting the master equation. Figure 2.1 depicts such a scenario, with the quantum system represented as a red circle with a nonlinear energy spectrum of some number of energy levels, whose output light is mixed with the input light, shown by the added red hue of the wave packet for a_{out}^R as compared to a_{in}^R. For the two-level system with Hamiltonian considered in 2.1.1, after mak-

ing the approximations mentioned and given in detail in [25], the input-output relations are

$$a^R_{\text{out}}(\omega, t) = a^R_{\text{in}}(\omega, t) + e^{-i\omega_A t_A}\sqrt{\frac{\Gamma}{2}}\sigma_-(t - t_A) \tag{2.17}$$

The time constant $t_A = x_A/v$ is the time taken for the signal to reach the atom on the chip. As we are only focusing on a single transmon, we can set $t_A = 0$. The expression for the output field generalizes straightforwardly with the three-level atom as

$$a^R_{\text{out}}(\omega, t) = a^R_{\text{in}}(\omega, t) + \sqrt{\frac{\Gamma_0}{2}}\sigma^{(0)}_-(t - t_A) + \sqrt{\frac{2\Gamma_0\omega_{(2,1)}}{2\omega_{(1,0)}}}\sigma^{(1)}_-(t - t_A) \tag{2.18}$$

Thus, we can relate the measured modes a_{out} to the system of interest-namely, the atom. The next sections discuss more in detail how to relate measurements to the atomic system parameters.

2.3 Transmission and reflection of the sample

The transmission and reflection coefficients can be measured via spectroscopy through the waveguide. In the language of input-output theory [25]:

$$t = \frac{\left\langle a^{(R,L)}_{\text{out}} \right\rangle}{\left\langle a^{(L,R)}_{\text{in}} \right\rangle} \tag{2.19}$$

$$r = \frac{\left\langle a^{(L,R)}_{\text{out}} \right\rangle}{\left\langle a^{(L,R)}_{\text{in}} \right\rangle} \tag{2.20}$$

By the linearity of the expectation value and substituting equation 2.17, we know

$$\left\langle a^R_{\text{out}} \right\rangle = \left\langle a^R_{\text{in}} \right\rangle + \sqrt{\frac{\Gamma}{2}} \left\langle \sigma_- \right\rangle .$$

Thus, using the master equation to describe the population dynamics of the atom, we can determine the steady-state solution of $\left\langle \sigma^{(0,1)}_- \right\rangle$ by solving the linear system of equations formed by the vectorized atomic density matrix, known as the Optical Bloch equations [42]. In practice, this is done by vectorizing the Liouvillian $\mathcal{L}(\rho)$ and solving for the null space in *Mathematica*. Once we have the steady state solution for the density matrix elements, we recall $\langle \sigma_- \rangle = \text{Tr}\{\rho\sigma_-\}$ to determine $\langle \sigma_- \rangle$.

The master equation (2.5) included only spontaneous emission into the waveguide as the dissipative element. However, we care about other environmental effects on the atom, namely dephasing and non-radiative decay, whose origins are an active field of research. One can also include thermal excitation. To

obtain a fit function for the transmittance and reflectance of the setup, I will add the dissipators $\mathcal{D}(A,\rho) \equiv A\rho A^\dagger - \frac{1}{2}\{\rho, A^\dagger A\}$ with non-radiative decay rate Γ_{nr} and dephasing Γ_ϕ as in [42] such that the master equation $\dot{\rho} = \mathcal{L}(\rho)$ for the two-level transmon in the transmission line is

$$\dot{\rho} = \mathcal{L}(\rho) = -\frac{i}{2}[H,\rho] + \Gamma_0\mathcal{D}(\sigma_-^{(0)},\rho) + \Gamma_{\text{nr}}\mathcal{D}(\sigma_-^{(0)},\rho) + \frac{\Gamma_\phi}{2}\mathcal{D}(\sigma_z^{(0)},\rho) \tag{2.21}$$

With this master equation, we obtain $\langle\sigma_-\rangle$ in steady state, and then with input-output theory, we can solve for $\left\langle a_{\text{out}}^{(L,R)}\right\rangle$ and substitute into equation (2.20) to obtain

$$r = \frac{\eta\Gamma_0}{\Gamma_0 + 2\Gamma_\phi}\frac{1 - i\delta\omega/\left(\Gamma_0/2 + \Gamma_\phi\right)}{1 + \left(\delta\omega/\left(\Gamma_0/2 + \Gamma_\phi\right)\right)^2 + \Omega_0^2/\left(\Gamma_0\left(\Gamma_0/2 + \Gamma_\phi\right)\right)} \tag{2.22}$$

where $\eta \equiv \Gamma_0/(\Gamma_0 + \Gamma_{\text{nr}})$ is the ratio of radiative to total decay rate, including non-radiative components. The transmission coefficient $t = 1 - r$ due to the requirement to satisfy Kirchhoff laws [41].

2.4 Field correlations and power spectral density

The previous section detailed how to use input-output theory to determine expectation values of the output field to determine transmission and reflection coefficients which are measured in spectroscopy. The challenge and exciting undertaking extending such studies is the measurement of multi-time field correlations derived from moments of the field, which allow us to glean more information about the quantum interactions between the atom and the electromagnetic modes.

For any complex-valued signals w and v, the cross-correlation function of the signals is defined as

$$(w \star v)(\tau) \equiv \int_{-\infty}^{\infty} w^*(t)v(t+\tau)dt \tag{2.23}$$

$$= \langle w^*(t)v(t+\tau)\rangle\,, \tag{2.24}$$

where $\langle\cdot\rangle$ denotes the time-average. For signals of interest, we assume a stationary and ergodic system, meaning ensemble averages are equivalent to time-averages (see [30] and references therein), and the particular time t at which the averaging starts is irrelevant. With these conditions, ensemble averages of finite-time averages are equivalent. The first-order normalized autocorrelation function for signal s is then defined as

$$g^{(1)}(\tau) = \frac{\langle s^*(t)s(t+\tau)\rangle}{\langle s^*(t)s(t)\rangle} \tag{2.25}$$

The signature of any nonlinear element, distinguishing atoms from cavities, is incoherent scattering. That is, when driving the system at frequency ω_A , how

is this energy redistributed in frequency? This contrasts from spectroscopy first in that incoherently scattered radiation has $\langle a \rangle = 0$, but $\langle a^\dagger a \rangle > 0$, while this is not the case for coherently scattered radiation. The Wiener-Khinchine theorem relates the power spectral density (PSD), denoted $\mathcal{S}(\omega)$, to the auto-correlation function of the signal. Thus, to learn about the power spectrum, we measure $g^{(1)}(\tau)$. Appendix B.1 details this relationship in more detail. Therefore, by determining the auto-correlation function of the field mode, we gain further insight into the structure of the source of the field, namely the atom via its lowering operator as seen in section 2.2.

2.4.1 Measuring first-order correlations

In practice, we measure discrete time-traces of electric fields obtained by mixing the signal output from the sample, discussed in chapter 3.2, via heterodyne detection. In this thesis, I will denote continuous signals s as $s(t)$ and discrete signals as $s[t]$, following [28]. The quantum-mechanical field a of interest is complex-valued, however, and therefore non-Hermitian and so knowing both amplitude and phase of a is impossible by the Heisenberg uncertainty principle. How we then determine a via measured electric fields is outlined in [28], but I'll outline the reasoning. Mixing is described by a beam splitter which outputs the in-phase component of the field I and the out-of-phase component Q, with one input being the quantum field $a = I_a + iQ_a$ and the other being the vacuum or a weak thermal state h. The outputs of the beam splitter are $c = (a + h)/2$ and $d = (a - h)/2$. Then, measuring one of the quadratures of these outputs gives $I = (c + c^\dagger)/2$ and $Q = -i(d - d^\dagger)/2$. These outputs do commute, and so we can measure both to obtain a signal $S = I + iQ = (a + h^\dagger)/\sqrt{2}$, where both quadratures are now measurable. This came at the cost of introducing noise to the field, $h^\dagger$. This is minimally vacuum uncertainty, but could be other noise as well, depending on the physical nature of the mixing process.

In practice, before mixing we amplify the signals emitted by the sample with a linear amplifier, as they are much too small for a digitizer to detect. Thus, the signal we measure is related to the original mode of interest by $S = \sqrt{g}(a + h^\dagger)$, where $g = P_{\text{out}}/P_{\text{in}}$ is the gain of the amplification line. Therefore the dominant noise source in our signals is the added noise due to the amplifiers with non-unit gain. See [9] for the original description of a quantum linear amplifier, or [10] for a recent review.

So to extract correlations of the mode a of interest, we must account for the noise $h^\dagger$ added by mixing and amplification. The cross-correlations of any discrete waveforms w and v, denoted $(w \star v)[\tau]$, is

$$(w \star v)[\tau] \equiv \sum_{t=0}^{T-t_s} w^*[t]\, v[t + \tau \bmod T]\,. \tag{2.26}$$

To measure the correlation function of the signal s in practice, we take ensem-

ble averages $\langle\cdot\rangle$, and we denote this measured first-order correlation as in [28]:

$$\begin{aligned}\Gamma^{(1)}[\tau] \equiv \langle s \star s\rangle &= g\left\langle (a+h^\dagger)\star(a+h^\dagger)\right\rangle \\ &= g\left(\langle a\star a\rangle + \left\langle h^\dagger \star h^\dagger\right\rangle + \left\langle a\star h^\dagger\right\rangle + \left\langle h^\dagger\star a\right\rangle\right) \\ &= gG^{(1)}[\tau] + H^{(1)}[\tau]\end{aligned} \tag{2.27}$$

with the definitions

$$G^{(1)}[\tau] \equiv \left\langle a^\dagger(t)a(t+\tau)\right\rangle \tag{2.28}$$

$$H^{(1)}[\tau] \equiv g\left\langle h(t)h^\dagger(t+\tau)\right\rangle \tag{2.29}$$

being the unnormalized auto-correlations of the field and noise, respectively. Thus, we find

$$gG^{(1)}[\tau] = \Gamma^{(1)}[\tau] - H^{(1)}[\tau] \tag{2.30}$$

So, we can subtract an "off" measurement $H^{(1)}[\tau]$ to determine the first order correlations of mode a. A good reference for added noise during amplification at the quantum level is [9].

2.4.2 The dressed two-level system and the Mollow triplet

The field correlations $\left\langle a^\dagger(t)a(t+\tau)\right\rangle$ of the light emitted by a two-level system employs similar methods as the transmission and reflection coefficients in section 4.1, but one additional tool is needed: the quantum regression formula [8]. The quantum regression formula reads, for a two-time correlation of mode a,

$$G^{(1)}(\tau) = \left\langle a^\dagger(t)a(t+\tau)\right\rangle = \operatorname*{Tr}_S\{ae^{\mathcal{L}\tau}\left[\rho(t)a^\dagger\right]\}, \tag{2.31}$$

where $\operatorname*{Tr}_S\{\cdot\}$ denotes the trace over the system S. Thus, we need only the input-output relations and the Liouvillian governing the dynamics of the atomic state populations (the optical Bloch equations) via the master equation (2.5) to determine $g^{(1)}(\tau)$, and from there, use the Wiener-Khinchine theorem to obtain the power spectrum of the driven two-level atom. Here, we consider the resonantly driven two-level system Hamiltonian in the rotating frame of the drive, given by (2.8) with $\delta\omega = 0$. The result under such conditions gives the power spectral density $\mathcal{S}(\delta\omega)$ of an atom driven strongly and near-resonant, given by

$$\mathcal{S}(\delta\omega) = \frac{8\Gamma^2\Omega^4\left(2\left(\Gamma^2+\delta\omega^2\right)+\Omega^2\right)}{\left(\Gamma^2+4\delta\omega^2\right)\left(\Gamma^2+2\Omega^2\right)\left(\Gamma^4+\Gamma^2\left(5\delta\omega^2+4\Omega^2\right)+4\left(\delta\omega^2-\Omega^2\right)^2\right)} \tag{2.32}$$

Note in this equation we have removed the coherent delta function due to the drive tone. A visualization and plot of the spectrum is given in figure 2.2. At high Rabi rates, the spectrum splits into three peaks, which gives it the name:

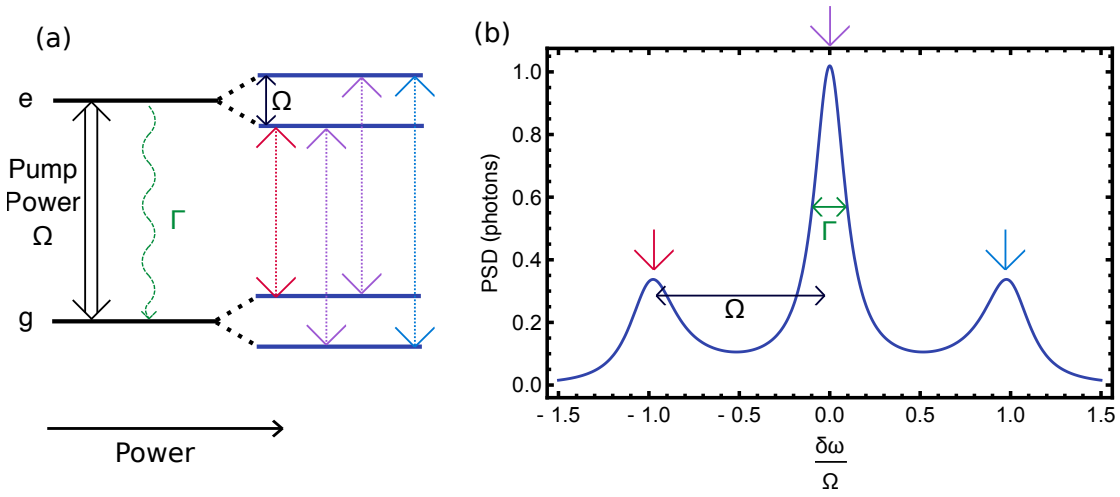

Figure 2.2: The dressed states and Mollow triplet. (a) Energy level diagram of the two-level atom driven by a strong drive (double arrow). The increasing drive power dresses the atomic states with the optical mode. (b) Power spectral density under strong drive. Ω gives the splitting of the dressed states, and radiative linewidth Γ is the full-width at half-maximum of the central peak.

the *Mollow triplet*, after Mollow's calculation of it in [31]. The level splitting shown in figure 2.2 (a) indicates a dressing of the atomic states, but this requires some clarification. The fact is that the atom-field collective quantum state $|n_{\text{atom}}\rangle\,|n_{\text{field}}\rangle$ is splitting its degeneracy. In reality, under resonant drive, the atom-field Hamiltonian has degenerate eigenstates: $H\,|n+1,g\rangle = H\,|n,e\rangle$. But the coupling Hamiltonian $H_I = \hbar\Omega/2(a\sigma_+ + a^\dagger\sigma_-)$ splits the atom-field state into eigenstates $|n,\pm\rangle = (|n,e\rangle \pm |n,g\rangle)/\sqrt{2}$, with energy difference $\hbar\Omega\sqrt{n}$. At very large drive field photon number n, the difference in the splittings of the levels $|n,\pm\rangle$ and $|n+1,\pm\rangle$ is small, as $\sqrt{n} \approx \sqrt{n+1}, n \gg 1$. Thus, the dressed-state "ladder" at high photon number shows a splitting of the form in figure 2.2 (a). One can take the Hamiltonian in equation (2.8), calculate the eigenvalues, and understand that at high n, the splitting in the dressed-atom field states for the drive with n photons is about the same as that for the dressed states with $(n+1)$ photons, and so we have an effective four-level system from what had appeared to be only two when only the atom degrees of freedom were considered.

2.4.3 Three level dynamics under two-photon drive

Considering the third level of the transmon could also show interesting field and photon correlation effects. Previous works have explored using the third level of the transmon and performed two-tone spectroscopy, revealing the Autler-Townes splitting. This is the effect observed when a three-level quantum system is strongly driven in one transition, and a splitting is observed at the other transition. By using two-tone spectroscopy, prior works [4, 38] had measured this splitting which we theoretically see in figure 2.3. Furthermore, prior work [24] has driven a transmon qubit in an open transmission line at the g-f/2 transition, measuring the three-state dressed states which occur for transmons with weak anharmonicity. The most efficient way to induce

transitions is to pump them directly at the frequency of the transition. These transitions lead to the absorption of a single energy quantum by the system. However, because the pump frequency is the same as the signal frequency, the pump radiation and the radiation emitted by the transition will superimpose, obfuscating the nonclassical statistics of the light emitted by the two-level system. To circumvent this, one can pump a second-order transition by driving at half the energy between the $|g\rangle$ and the $|f\rangle$ state; this is denoted the "two-photon drive", because two photons would need to be absorbed to meet the energy required by this transition. Note that a direct transition is not allowed, as the dipole coupling only allows changes by a single excitation [24]. The "two-photon" drive works via a virtual excitation via the $|e\rangle$ state. By populating the $|f\rangle$ state with the two-photon drive and monitoring the outgoing signal around the e-f transition or the g-e transition, we would obtain be able to measure the light statistics of the transmon without the coherent pump tone interfering.

As a step towards measuring photon correlations with the two photon drive, we first examine the field correlations of the system. This is done analogously to 2.4.2, except we take the three-level Hamiltonian in equation (2.15) and set $\omega_d = \frac{1}{2}(\omega_{ge} + \omega_{ef})$. In matrix form, this gives

$$H = \hbar \begin{pmatrix} 0 & \Omega_0/2 & 0 \\ \Omega_0/2 & -\alpha/2 & \sqrt{2}\Omega_0/2 \\ 0 & \sqrt{2}\Omega_0/2 & 0 \end{pmatrix} \tag{2.33}$$

By solving for the three-level optical Bloch equations and applying equation 2.31 as before, we numerically calculate the spectrum obtained from the two-photon drive and offer a comparable dressed-state picture as was done in the two-level resonant case.The two-photon drive of the transmon is shown in figure 2.3. Part (a) shows the first the levels of the transmon with anharmonicity $\alpha = \omega_{ef} - \omega_{ge} < 0$ with a drive tone (double arrow) at half the energy of the g-f transition, $\omega_{gf/2}$. Relative to $\omega_{gf/2}$, $\omega ef = \omega_{gf/2} - |\alpha|/2$, and $\omega_{ge} = \omega_{gf/2} + |\alpha|/2$. As power of the tone is increased, as with the qubit case in section 2.4.2, the undriven states are dressed with the strong drive tone, splitting the two levels which are driven resonantly (here, in second-order). This results in seven distinct transitions, which are shown in the peaks of the power spectral density plots in figure 2.3 (b). The detuning is relative to $\omega_{gf/2}$ such that $\delta\omega = (\omega - \omega_{gf/2})$, normalized to the anharmonicity. The e-f transition is found at $-|\alpha|/2$ relative to $\omega_{gf/2}$, and the g-e transition is found at $|\alpha|/2$. The low-power transitions, denoted by the colored vertical lines, match the dotted colored lines in part (a), showing the frequency shift and splitting which results from the strong two-photon drive. Note the difference in amplitude of the e-f and g-e transitions as compared to the (g-f)/2 transition. This illustrates the smaller likelihood of the second order process. Note the coherent pump tone is not shown in these plots, but would be a delta peak at its drive frequency, $\omega_{gf/2}$. A stronger drive power further shifts the e-f transition down in frequency (top plot), and the g-e transition up in frequency, as well

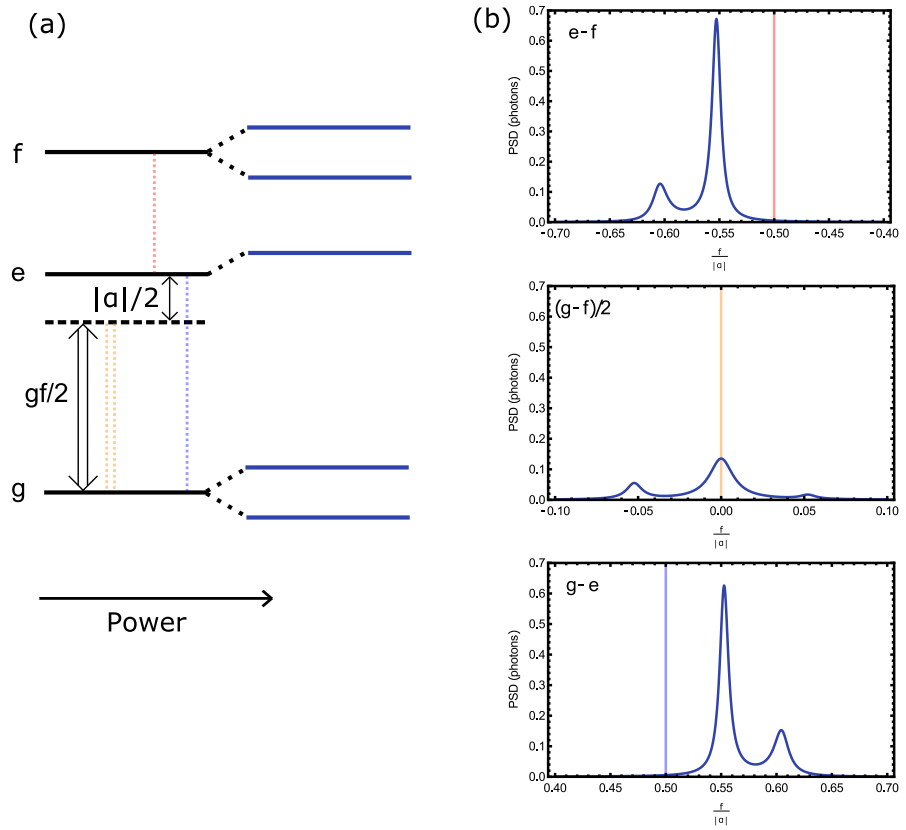

Figure 2.3: The dressed states from a two-photon drive. (a) Energy level diagram of the three-level transmon driven by a strong two-photon drive (double arrow). The increasing drive power dresses the three states. (b) Power spectral density of each transition. Vertical lines correspond the low-power transitions denoted in (a).

as broadening the splitting between the two transitions. The former is understood as a Stark shift by the non-resonant coupling of the drive to the $|e\rangle$ state, and the latter to be analogous to the splitting in the two-level system case. The power dependence of the two-photon drive is shown in figure 2.4. The upper plot centers on the ω_{ge}, while the lowest shows the PSD at frequencies around ω_{ef}, and the center shows the $\omega_{gf/2}$. The power Ω is in units of the g-e linewidth, Γ.

2.5 Photon correlation functions

The second-order (i.e. photon, or intensity-intensity) correlation function is the de facto quantity to determine the "quantumness" of the light source. The celebrated photon anti-bunching behavior of single emitters defied any classically allowed source of light. The second-order correlation function of the field is given by

$$G^{(2)}(\tau) \equiv \left\langle a^\dagger(t)a^\dagger(t+\tau)a(t)a(t+\tau)\right\rangle = \underset{S}{\mathrm{Tr}}\{a^\dagger a e^{\mathcal{L}\tau}\left[a\rho(t)a^\dagger\right]\}, \qquad (2.34)$$

with the second equality given by the four-operator extension of the quantum regression formula. Note also the normal ordering of the operators in

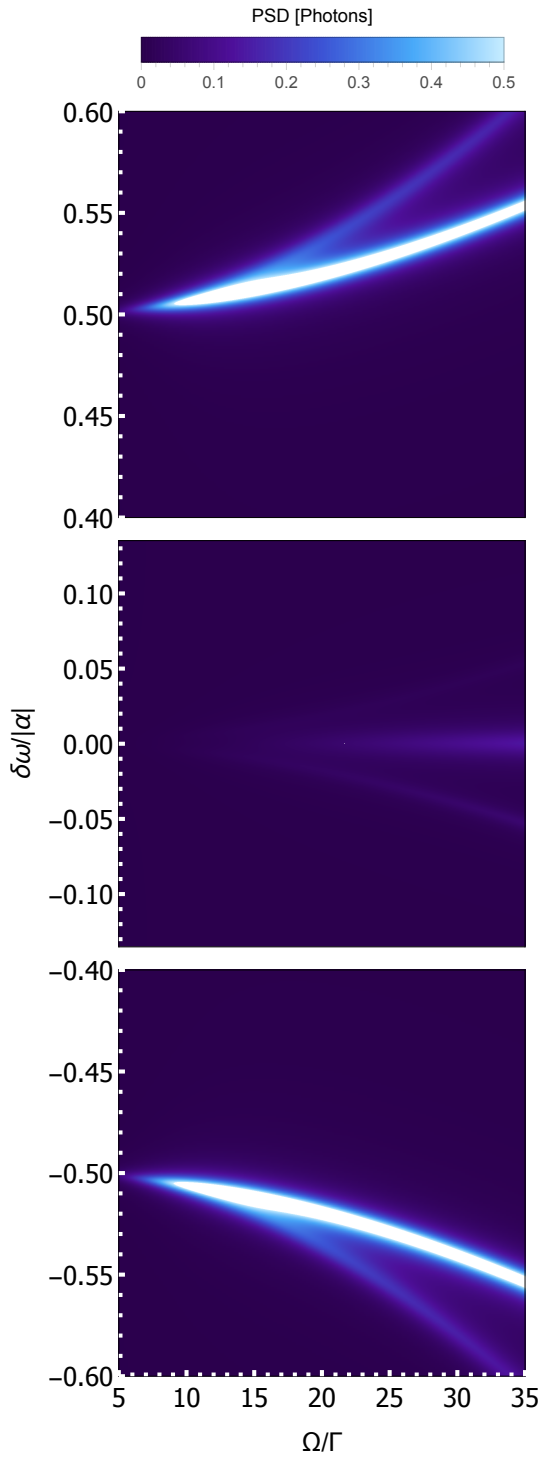

Figure 2.4: Power Spectral Density of a three-level atom under a two-photon drive of varying power.

the middle expression; this is due to the quantum-mechanical nature of photodetection; namely, by photon absorption. The canonical measurement of intensity correlations uses the Hanbury-Brown-Twiss interferometer, which measured photon number twice, one delayed in time by the other by τ. Thus, normal ordering describes the fact that, quantum-mechanically, the measurement of a photon in the light field depletes the field by a single photon, while in the classical case, this remains the same. This is seen mathematically, as the expected value of this middle expression in equation (2.34) is $\langle n\,(n-1)\rangle$, indicating the detection of n photons, and then $(n-1)$ photons. Discussion of this point is motivated from [30] in section [5.10]. The expressions for $G^{(2)}(\tau)$ are obtained analogously as they were for $G^{(1)}(\tau)$, by using the master equation to obtain the optical Bloch equations, and substituting these relations into the quantum regression formula.

2.5.1 Distinguishing classical and quantum light sources with photon correlations

As was briefly mentioned in the previous section, photon correlations are the clearest indication of whether or not a signal is "quantum". This can be thought about well in terms of the underlying statistical distributions generating different light sources. For a thorough and satisfying delineation about the different types of second-order correlations, see [30].

A coherent light source is one generated by a laser or a microwave function generator. It is also the eigenstate of the anihillation operator and can be written:

$$|\alpha\rangle = e^{-|\alpha|^2/2} \sum_{n=0}^{\infty} \frac{|\alpha|^{2n}}{n!} |n\rangle\,, \tag{2.35}$$

where $|n\rangle$ is the Fock state with n photons. The brackets in equation 2.34 are taking the expectation value of the operators inside. If we consider $G^{(2)}(0)$ for a coherent state α, and we know $a\,|\alpha\rangle = \alpha$ and $\langle\alpha|\,a^\dagger = \alpha^*$, we get

$$\langle\alpha|\,a^\dagger a^\dagger a a\,|\alpha\rangle = |\alpha|^4 = \langle n\rangle^2\,. \tag{2.36}$$

Because the probability of measuring Fock state $|n\rangle$

$$\begin{aligned} P(n) = \langle n|\alpha\rangle &= e^{-|\alpha|^2/2} \sum_{n'=0}^{\infty} \frac{|\alpha|^{2n'}}{n'!} \langle n|\,|n'\rangle \\ &= e^{-|\alpha|^2/2} |\alpha|^2 \frac{|\alpha|^{2n}}{n!} \end{aligned} \tag{2.37}$$

follows a Poisson distribution, these are called *Poissonian* photon statistics. Furthermore, it can be shown that Poissonian distributions have equal mean and variance, that is $\langle n\rangle = (\Delta n)^2 \equiv \langle n^2\rangle - \langle n\rangle^2$. By expressing $G^{(2)}(\tau)$ in

terms of the photon number variance

$$\begin{aligned} G^{(2)}(0) = \left\langle a^\dagger a^\dagger a a \right\rangle &= \left\langle a^\dagger (a a^\dagger + 1) a \right\rangle \\ &= \left\langle n^2 - n \right\rangle \\ &= (\Delta n)^2 + \langle n \rangle^2 - \langle n \rangle \end{aligned} \tag{2.38}$$

we can gain insight into how $G^{(2)}(\tau)$ differs for different statistical distributions governing light generation. One can again see from this that $G^{(2)}(0) = \langle n \rangle^2$ for Poissonian light.

A perhaps more ubiquitous form of light is *thermal* light, which follows Boltzmann statistics in the classical sense. That is,

$$P(n) = \frac{e^{-\hbar\omega n / k_B T}}{Z} = \frac{\langle n \rangle^n}{(1 + \langle n \rangle)^{n+1}}, \tag{2.39}$$

where $Z = \sum_n \exp(\hbar\omega n / k_B T)$ is the partition function. One can show the second equality [30], and that this means the variance $(\Delta n)^2 = 2 \langle n \rangle^2$. Thus, using equation 2.38, we see that for thermal light $G^{(2)}(0) = 2 \langle n \rangle^2$. This means that for thermal light (and in fact any classically formulated light distribution), $g^{(2)}(0) \geq 1$. Specifically for thermal and other sources of "chaotic" light [30], $g^{(2)}(\tau) \leq 2$.

The quantum nature of light produces statistics entirely disallowed by classical physics. From our knowledge about the theory, we can see that this comes about by the fact that, for single photons, the expectation value $\langle n(n-1) \rangle = 0$. One sees this by carrying out the same calculation for Fock state $|1\rangle$ as was done for coherent states:

$$G^{(2)}(0) = \langle 1 | a^\dagger a^\dagger a a | 1 \rangle = \langle 0 | a^\dagger a | 0 \rangle = 0 \tag{2.40}$$

Thus, single photons as mathematically described can produce $g^{(2)}(0) < 1$; this is called *sub-poissonian* light. Intuition for this idea can be seen by considering the paritcle nature of light. The correlation $g^{(2)}(\tau)$ can be thought about as the relative likelihood that, conditioned on the fact that you've already seen a photon (mathematically embodied by the two a's in $\left\langle a^\dagger a^\dagger a a \right\rangle$), what is the likelihood you will see another one time τ afterwards? For a single-photon source, this must be less likely ($g^{(2)}(\tau) < 1$ for small τ), and is in fact 0 at $\tau = 0$, for a single-photon source by definition cannot emit two photons at the same time.

Thus, the observation of sub-Poissonian statistics defines the non-classical light source. By considering interference effects of a single photon source with traveling resonant light, one can also predict superbunching ($g^{(2)}(\tau) > 2$) for quantum systems, though in principle there is no mathematical limit, like the Cauchy inequality for antibunching, barring a classical light source from exhibiting super-bunching effects as well [30] it certainly does not occur naturally

like chaotic light statistics do, and reflects constructive interference which are often most accurately described by quantum-mechanical origins.

Thus, to measure nonclassical light means to measure photon anti-bunching. Measuring super-bunching also strongly suggests it, and also distinguishes the light from either coherent or thermal light sources.

2.5.2 Measuring photon correlations with linear detection

The procedure to measure $G^{(2)}(\tau)$ from discrete, noisy time-traces is similar, but more involved, than the case for first-order correlations in section 2.4.1. To extract the field mode correlations $G^{(2)}[\tau]$ from a signal $s[t] = a + h^\dagger$, we must measure four quantities: $\Gamma^{(1)}[\tau]$ and $H^{(1)}[\tau]$ as defined in equations (2.27) and (2.28), and their second-order counterparts

$$\Gamma^{(2)}[\tau] \equiv g^2 \left\langle s^\dagger s \star s^\dagger s \right\rangle \tag{2.41}$$

$$H^{(2)}[\tau] \equiv g^2 \left\langle h h^\dagger \star h h^\dagger \right\rangle \tag{2.42}$$

By expressing s in terms of field mode of interest a and the added noise $h^\dagger$ present by amplification and other processes in the measurement line, substituting into equation (2.34), and assuming that all terms involving odd powers of the noise operators are 0 (as $\langle h \rangle = 0$), we obtain the normalized second order correlation function $g^{(2)}[\tau]$

$$g^{(2)}[\tau] = \frac{G^{(2)}[\tau]}{|G^{(1)}[0]|^2} \tag{2.43}$$

where

$$\begin{aligned} g^2 G^{(2)}[\tau] = \Gamma^{(2)}[\tau] - H^{(2)}[\tau] - \\ 2g G^{(1)}[0] H^{(1)}[0] - \\ g G^{(1)}[-\tau] H^{(1)}[\tau] - \\ g G^{(1)}[\tau] H^{(1)}[-\tau] \end{aligned} \tag{2.44}$$

We are thus equipped to extract the photon correlations of the field output from the wQED system and probe the non-classical properties of artificial atoms in the waveguide. The next chapter delves into the experimental work done over the course of this thesis to measure amplitude and intensity (i.e. photon) correlations for transmons embedded in a coplanar waveguide.

Chapter 3

Experimental methods

There are several important experimental tools and techniques that are used to measure correlations of non-classical microwave light: the dilution refrigerator, which prepares the thermal and electrical environment for the artificial atoms, the signal engineering and processing used to measure the correlations, and the Josephson parametric amplifier used to reduce the added noise due to amplification as much as possible. This chapter provides an overview of each and details important to the understanding of the measurements given in chapter 4.

3.1 The cryogenic setup

The workhorse of circuit QED and many fields requiring low-temperatures is the dilution refrigerator cryostat. Our dilution refigerator consists of six plates which are cooled to successively lower temperatures; nominally, they are 300 K, 70 K, 4 K, 1 K, 100 mK, and 40 mK. Figure 3.1 shows the 4 K plate and below of the cryostat. The cooling mechanism uses a mixture ^{4}He and ^{3}He, taking advantage of the superfluidity of ^{4}He and the lower boiling point of ^{3}He to perform evaporative cooling on the mixing chamber at the base plate. The Vericold dilution refrigerator used in this experiment additionally employs pulse-tube technology such that the gas-handling circuit is closed, thus not requiring any refilling of ^{4}He. The interested reader can find details on the operation and physical basis of cryogenics in [34]. This type of cryostat brings temperatures below 40 mK in reach, or about 0.4% and 3.3% of the nominal T_c of niobium and aluminum, respectively. At these temperatures, the quantum nature of the circuits is manifest and measurable. To measure and characterize our superconducting quantum circuits, however, we must electrically connect them to the room-temperature environment, without compromising the temperatures achieved using the cryostat. A schematic of the cryogenic wiring used for the wQED experiment is shown in figure 3.2. Depicted are the different temperature stage plates on the left, and the microwave coaxial cables denoted by thick black lines. The 30 μm superconducting coil DC wires are denoted by the thin twisted pair of dashed lines. The DC wires biasing

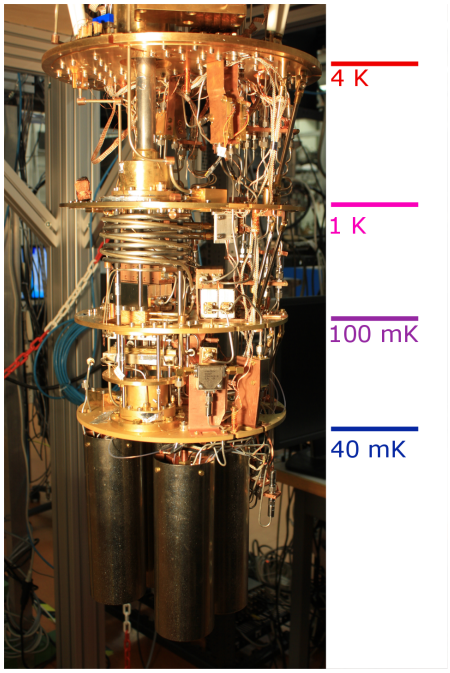

Figure 3.1: Image of the cryostat used for measuring the wQED sample. The different temperature stages are indicated next to the plates shown in the photograph.

the High Electron-Mobility Transistor (HEMT) amplifiers are not shown. To enable measurement of the sample in transmission and reflection from both ports of the waveguide, circulators with 20 dB isolation are placed at either side of the chip, which also prevents the formation of standing waves in the line that could heat the sample and the cryostat. The band-pass filters before the HEMT amplifiers at 4 K prevent any high-power spectral noise outside the band of interest from compressing the amplifier. To prevent an unwanted thermal link, all cables which cross a thermal stage are either stainless-steel or superconducting, while to minimize added noise at the sample, all cables are copper below the base (40 mK) plate. Stainless steel cables are used for all input lines despite their poorer electrical properties in order to reduce the heat load on the cryostat. The output lines have stainless-steel cables in place after the HEMT amplifiers and either superconducting or steel cables between all temperature stages. Additionally, DC blocks are placed at all microwave line inputs at the top flange of the cryostat to ensure coupling into the measurement lines is only AC, preventing voltage differences between grounds, which could cause unwanted heating of the system.

We must also consider decoherence of the quantum circuits due to thermal noise and reduce heat load on the cryostat. To reduce the heat load, we short the thermal link made by microwave lines which go to the sample by thermalizing the outer conductor of the coaxial cable at several points between the top flange and the base plate (not indicated in figure 3.2). To both reduce Nyquist noise and prevent a thermal link by the inner conductor of the cable, we thermalize the inner conductor of the cables by placing three 20 dB attenuators in the signal input lines, which are thermalized at the 4 K, 100 mK, and

40 mK temperature stages of the setup, indicated by the blue symbol in figure 3.2. Assuming spectrally white Nyquist noise, the power spectral density is $\mathcal{S}_{\text{noise}}(\omega) = 4k_{\text{B}}T/\hbar\omega$ photons for any given mode, where ω is the frequency of the mode the photons are occupying (see appendix B.3). Assume we operate at frequency $\omega/2\pi = 6\,\text{GHz}$. Then, 300 K Nyquist noise corresponds to 4167 noise photons. At the bottom of the microwave input line, we have attenuated the 300 K noise by 1 million (60 dB), so this contributes $n_{\text{RT}} \approx 0.004$ photons to the noise at base temperature. However, the three attenuators, thermalized at different stages of the line, also add their own noise: 4 K attenuated by 40 dB, 100 mK attenuated by 20 dB, and unattenuated 40 mK noise. At base, these then add 0.005, 0.013, and 0.55 noise photons at 6 GHz, respectively. That is, this attenuation scheme leaves the dominant noise source the base temperature noise, by a factor of 500 over the second largest noise source. This attenuation setup is quite important for minimizing the thermal noise which would interact with the transmons, reducing their quantum coherence.

Aside from thermal noise interfering with the qubit, the added noise of the amplification chain will determine our signal quality. This is especially important for $g^{(2)}[\tau]$ measurements because of the exponential scaling of required averages to obtain a given accuracy as a function of the correlation order [11]. The HEMT amplifiers at the 4 K stage have a nominal noise temperature of 5 K, but in our experiments we have measured temperatures as high as 35 K. This discrepancy can be caused by a number of experimental factors, including quality of thermalization of the HEMT to the cryostat, or deviations in the optimal bias voltages yielding the desired drain current I_D of the HEMT as the HEMT is thermally cycled. Although HEMT operation should be nominal, the effect of sub-optimal HEMT operation can be reduced by employing a lower-noise amplifier before the HEMT. Using an ideal quantum-limited, phase-preserving parametric amplifier, one can achieve added noise of a single photon by the amplifier [9]. In practice, we have reduced the added noise of the total amplification chain to $\simeq 3$ added noise photons, corresponding to $\simeq 100\,\text{mK}$ of added noise (see figure 3.8). Note that another way to reduce added noise in $g^{(2)}[\tau]$ measurements, past experiments have used independent amplification chains and preformed the cross-correlation of intensities recorded from the two lines [20]. However, in this experiment, we use a measurement setup similar to [15] to measure $g^{(2)}[\tau]$, measuring from a single line with a phase-preserving Josephson parametric amplifier as the first amplifier in the chain (see figure 3.2).

Further cryogenic cabling measures are in place to operate the quantum-limited Josephson parametric amplifier, denoted by the amplifier symbol with the "JPD" text inside it, standing for "Josephson Parametric Dimer" [16]. To protect the transmons from the strong pump tones required to supply the energy to the JPD which amplifies the signal, two isolators are placed between the input-output circulator at the sample and the JPD output circulator. Though this increases the attenuation between the sample and the amplifier, reducing the signal-to-noise ratio (SNR), the insertion loss of the three circulators, in total measured to be $\simeq 1 - 1.5\,\text{dB}$ is thought to be sufficiently small in com-

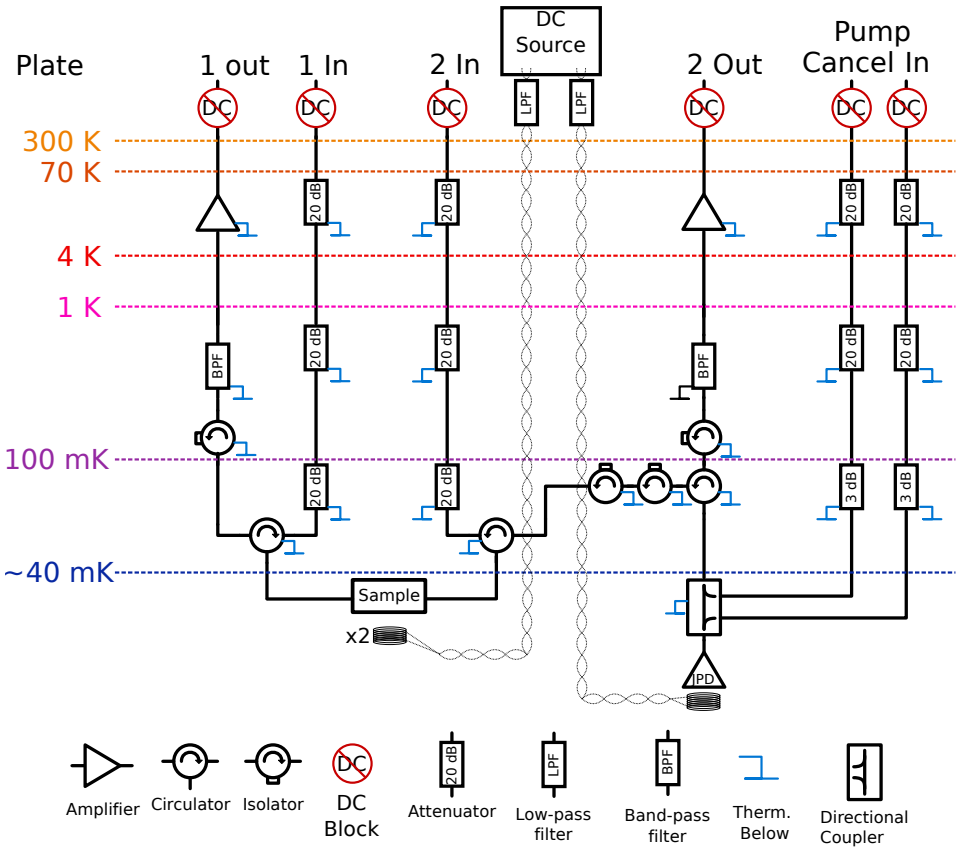

Figure 3.2: Schematic of the cryogenic microwave lines for measuring the wQED sample. Also shown are the DC coil wires which generate magnetic flux.

parison to the added benefit they offer of isolating the transmons from the strong pump tone. Appendix C compares the SNR of the output line with the JPD and the line without, illustrating the benefit of the JPD. Additionally, the pump tone is canceled interferometrically at the output of the directional coupler after the JPD, which provides another layer of protection for the sample from the pump tone. For a pump tone of 13 dBm at the microwave generator, the number of pump photons per second at the sample is estimated to be $\phi_{\gamma,\mathrm{pump}} \approx 0.23\,\mu\mathrm{s}^{-1}$ at the pump frequency $\omega_{\mathrm{pump}}/2\pi = 6.38\,\mathrm{GHz}$, given pump line attenuation to the sample $A_{\mathrm{pump}} \approx -112\,\mathrm{dB}$ and 35 dB of cancellation. Because $\omega_{ge} \neq \omega_{\mathrm{pump}}$, this population would not interact with the transmons in the experiment. The JPD is discussed further in section 3.4.

3.2 The quantum signal analyzer

The quantum signal analyzer is a warm electronics signal processing system which enables the efficient measurement of time-resolved moments of the microwave field, demonstrably up to second-order. It consists of two primary technologies: the analog down-conversion board, which converts the GHz-frequency signals to MHz-frequency, making digital sampling possible, and the Virtex 4 FPGA, which digitizes the signal and performs correlations of signals in real-time. The downconversion board performs heterodyne dete-

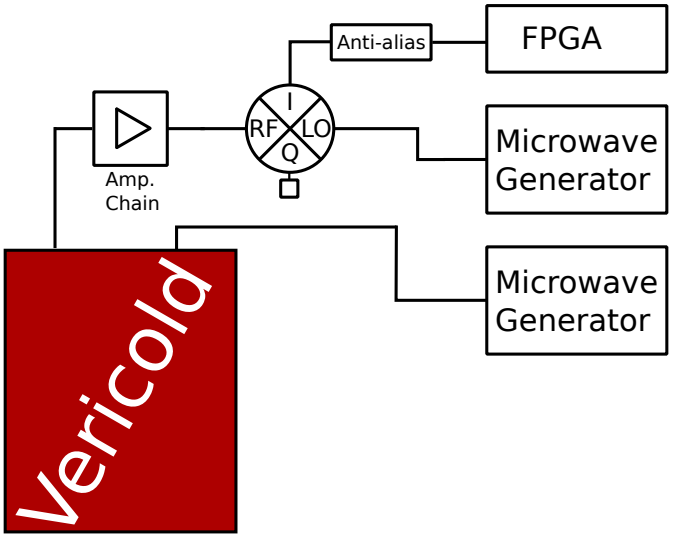

Figure 3.3: Schematic of signal processing into and out of the fridge for a single input and output (note two are used for the experiment). The LO signal is typically detuned from the input signal by 25 MHz. Only a single downconverted quadrature of the amplified signal exiting the cryostat is digitized.

tection with a frequency mixer, with the intermediate frequency ν_{if} being the difference between the signal frequency in the RF (radio frequency) port of the mixer and the local oscillator (LO), usually set to follow the RF input tone in CleanSweep at $\nu_{\text{LO}} = \nu_{\text{RF}} - 25\,\text{MHz}$. A schematic of the signal processing between the output of the cryostat is shown in figure 3.3. After downconversion to the intermediate frequency ν_{if}, the out-of-quadrature component of the signal (Q) is terminated, and the in-quadrature (I) part of the signal is filtered by an anti-aliasing low-pass filter with a 50 MHz cutoff frequency, the Nyquist frequency of the Virtex 4, which samples at $f_s = 100\,\text{MHz}$. The output is then digitized by the FPGA, digitally downconverted to DC, and the user can filter the data with a finite impulse response (FIR) filter and a moving-average (box-car) filter to further remove unwanted bandwidth. See appendix D for more information on how filtering affects realistic signals of known character. One notes that because only one component of the downconverted signal is saved, signals rotating at higher frequencies $\nu_{\text{sig}} = \nu_{\text{if}} + \delta$ are indistinguishable from the negative-frequency counterparts $\nu'_{\text{sig}} = \nu_{\text{if}} - \delta$. In other words, the frequency spectrum in the I quadrature must be symmetric around ν_{if}. This means that, if we want to measure the spectrum above the LO frequency at $\nu_{\text{sig}} = \nu_{\text{if}} + \delta$, we must ensure that the spectrum around $\nu\prime_{\text{sig}} = \nu_{\text{if}} - \delta$ contains no features, as these would appear at our frequency of interest upon taking a single quadrature of the signal. This is important for instance if one wants to interpret data obtained whilst sweeping the LO frequency. The quantum signal analyzer is discussed in further detail in [28].

Note that the schematic in figure 3.3 is simplified; in reality, the VirteX 4 has two analog-to-digital converter (ADC) inputs, which can then be manipulated together after digitization. The FPGA enables several "signal math" settings, in which one can take the amplitude, the intensity, or the auto-correlations

of either amplitude or intensity from one or two ADC channels and, due to details of the implementation on the FPGA board, the saved data is shifted by one or more bits relative to to the true measured values, necessitating a multiplication of the saved data by various powers of two, depending on the measurement. Specifically, for a signal S with units of V_{0-pk}, the following quantities relate to the saved CleanSweep signals denoted by S_{CS}:

$$\langle S[\tau]\rangle = 2\langle S_{CS}[\tau]\rangle \tag{3.1}$$

$$\langle S^*[\tau]\,S[\tau]\rangle = 4\langle S^*_{CS}[\tau]\,S_{CS}[\tau]\rangle \tag{3.2}$$

$$\langle S^*[0]\,S[\tau]\rangle = 16\langle S^*_{CS}[0]\,S_{CS}[\tau]\rangle \tag{3.3}$$

$$\langle S^*[0]\,S[0]\,S^*[\tau]\,S[\tau]\rangle = 64\langle S^*_{CS}[0]\,S_{CS}[0]\,S^*_{CS}[\tau]\,S_{CS}[\tau]\rangle \tag{3.4}$$

To read any correlation data, rather than pure amplitude or intensity data, one can use the `ReadCorrelatorData[]` function implemented in the `PhotonStateTomography`` *Mathematica* package. Alternatively, the data can be loaded using `ReadInData[]` in the `DataHandling`` package, and implementing a wrapper which normalizes the amplitudes of the signals according to equations (3.1) - (3.4).

3.3 The waveguide QED sample

To study correlations of nonclassical microwave light emitted by multiple transmons coupled in a transmission line, we studied a simple sample of two transmons coupled on either side of an uninterrupted meandering coplanar waveguide, as shown in figure 3.4. The chip itself is a 500 μm thick sapphire wafer with 150 nm of Nb patterned on top and bottom, which is etched away on top to create the waveguide center conductor and the areas where the transmons are placed. The transmons are designed to be separated by one wavelength at 6.5 GHz, and three-quarters of a wavelength at 4.875 GHz at their flux-tunable fundamental resonance, corresponding to 18.68 mm of waveguide length between them given the speed of light $v \approx 0.4c = 121.42\,\mathrm{mm\,ns^{-1}}$ in the coplanar waveguide. The transmons are fabricated from Aluminum via electron-beam lithography and shadow evaporation [13]. As indicated in the inset of figure 3.4 , the transmon capacitor width is 460 μm, and *Maxwell* simulations predict an $E_C \simeq 294$ MHz. By measuring the first and second resonances of the qubit and fitting these to the eigenfunctions of H_{CPB} in (1.8), we determined $E_C \simeq 320$ MHz for one qubit of the sample. This further gives an $E_J \simeq 16.5$ GHz. The meandering Niobium coplanar waveguide couples to the transmons capacitively with a separation of 76 μm between the central conductor and the transmon capacitor. This gives an expected coupling of $\Gamma_0 \simeq 2$ MHz. At the bends of the waveguide, and at either side of the meandering section, air-bridges connect the ground planes 4.5 μm separated on either side of the 10 μm-wide center line. Visible in figure 3.4 are the aluminum wirebonds which are electrostatically adhered to the chip and the copper printed circuit board (PCB).

After the sample is wire-bonded to the PCB, it is placed in a copper mount consisting of a base, a lid which is meant to prevent spurious microwave modes

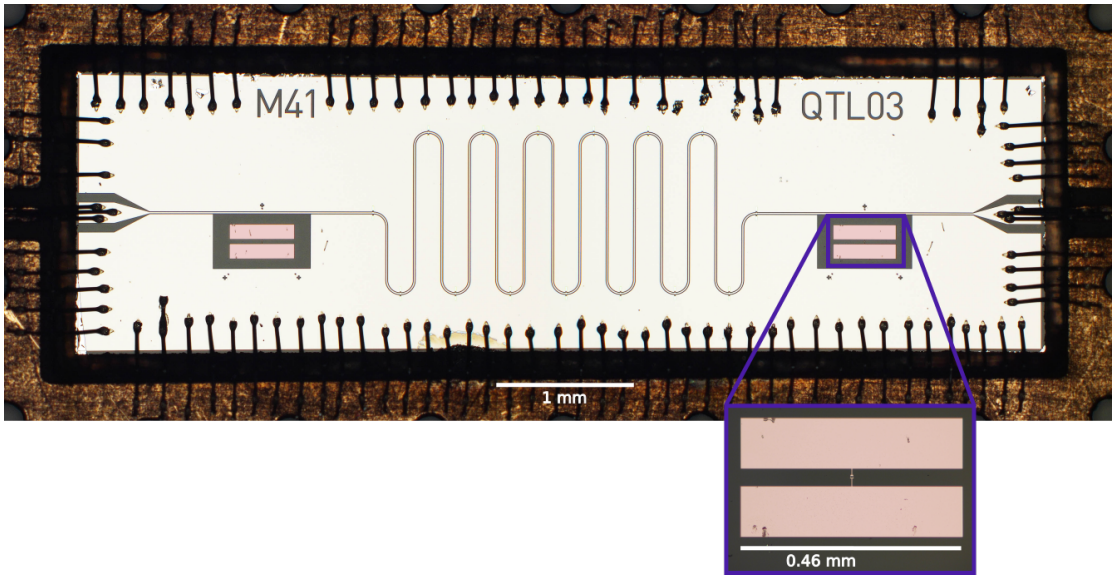

Figure 3.4: Optical micrograph of the wQED sample wirebonded to the printed circuit board. Transmons are false-colored red. Inset: close-up of one of the nominally identical transmons.

in the shield, and a copper cable mount to which one fastens the input cables, and also which thermalizes the sample to the base plate. The cables have SMP jacks which connect to the SMP jack launcher soldered onto the PCB via SMP plug "bullets". Once the sample is mounted in the setup, the coils are fastened to the copper base, and the sample is enclosed in two magnetically-shielding cylinders to prevent spurious magnetic fields from coupling to the device. In figure 3.1, the magnetic shields are in place around the sample mount, which is not shown.

3.4 The Josephson parametric dimer

Because of the exponential scaling of the number of averages required to achieve a given signal-to-noise ratio (SNR) with respect to the order of the microwave field being measured [11], obtaining a high signal-to-noise ratio is tantamount to probing the non-classical statistics in efficient time. Other works [6, 20] have used independent amplification chains, each with a commercial HEMT (High-Mobility Electron Transistor) as the first amplifier. This method relies on the independent noise properties of the amplifiers, to measure two-time correlation functions. Nonetheless, the Josephson parametric amplifiers are in principle quantum-limited in their noise properties, meaning the minimal added noise is due to the signal being mixed with the vacuum fluctuations inherent to the field, or half a quantum of noise for each quadrature [9]. This makes them superior amplifiers with which to probe higher order correlations in the microwave domain. Recently, Qudev [15] has used the Josephson Parametric Dimer (JPD) developed in [16] to measure photon correlations. In this section I detail how the amplifier used in our measurements is characterized and prepared for optimum use in measuring correlation functions.

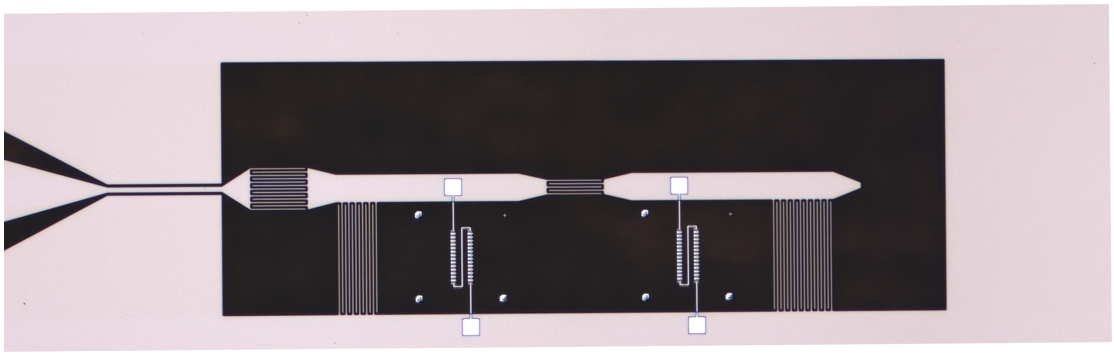

Figure 3.5: Optical micrograph of JPD7 1S 12, the quantum amplifier used to measure the wQED sample. Visible are the interdigitated capacitors and the SQuID arrays constituting the weakly nonlinear resonators.

The sample we have used is a Josephson Parametric Dimer, a micrograph of which is shown in figure 3.5. The JPD consists of two capacitively coupled, nominally identical lumped-element resonators with a weakly nonlinear inductance formed by a SQuID array. Each resonator has a finger-capacitor to the surrounding ground plane, and an array of SQuIDs with one meander that connects the central charge island to the ground plane. The nominally identical cavities form symmetric and antisymmetric normal modes ω_+ and ω_-, the splitting J being proportional to the coupling capacitance between the resonators. The symmetric and antisymmetric modes thus form the signal and idler modes of the parametric amplifier. The use of SQuIDs, rather than simply junction arrays, enables tunability via an externally applied magnetic field (see the coils in figure 3.2), similar to the case for the transmon. To determine the resonances of the JPD, a weak probe tone is input, and the phase of the reflection coefficient $\mathrm{Arg}\,[S_{11}]$ shows in high contrast the two resonances of the Dimer. One determines the phase by splitting the signal tone, such that one enters the cryostat and the other, called the *phase reference* is immediately downconverted and input into the second ADC of the FPGA, where the signal phases are the compared [16]. By changing the voltage of the superconducting coil below the JPD, one can tune the resonances, as shown in figure 3.6 (a). The tunability of the JPD allows us to center the amplification bandwidth onto the qubit resonance. The coil voltage working points we've used are $V_{JPD} = -800\,\mathrm{mV}$. Because we aim to have both qubits with resonance frequency $\omega_{q1} = \omega_{q2} = 2\pi \cdot 6.5\,\mathrm{GHz}$, the lower mode must serve as the signal mode, and the upper as the idler mode, as the higher-frequency mode cannot achieve our desired frequency.

Once we've selected the coil voltage, the two remaining parameters to set the JPD working point are set by the pump tone, which supplies the energy to amplify the signal tone. To preserve the phase of the signal after amplification, we chose to operate the JPD in *non-degenerate mode*. That is, we pump the JPD between the two resonances at $\omega_{\mathrm{pump}} = \omega_{\mathrm{signal}} + J = \omega_{\mathrm{idler}} - J$. The pump scheme is outlined in figure 3.6 (b). This achieves phase-insensitive amplification [16]. For most working points in this experiment we've used frequencies of $\omega_{\mathrm{pump}} = 2\pi \cdot 6.38\,\mathrm{GHz}$. Though the optimal pump power for coil voltage

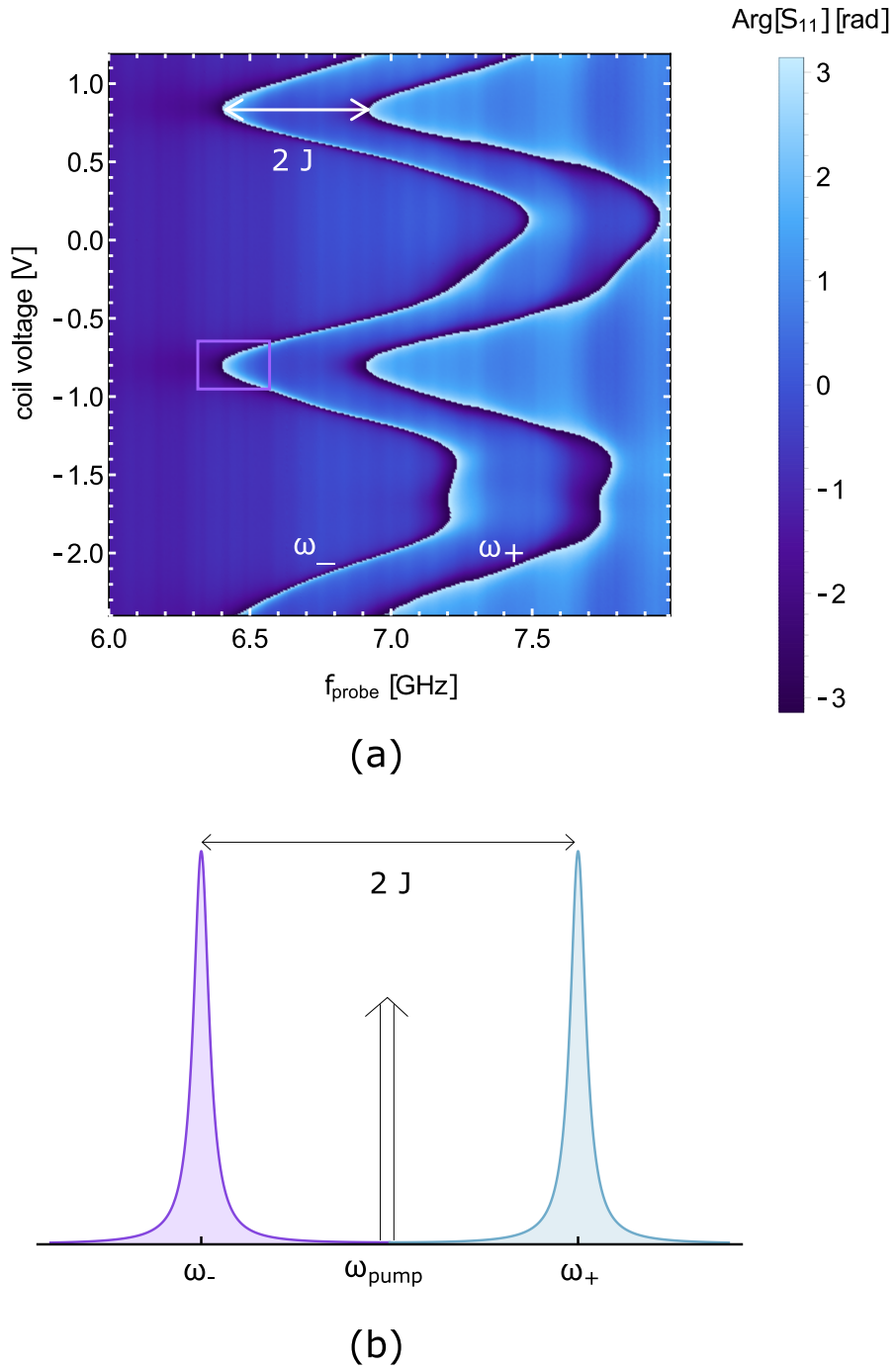

Figure 3.6: Methods to find a JPD setpoint. (a) The phase of the reflected signal of the JPD sample as a function of coil voltage to determine the desired coil voltage for the frequency range of interest (purple box). (b) Pump scheme for phase-insensitive amplification. The pump frequency is at the mid-point between the signal (purple) and idler (blue) mode. See text for details.

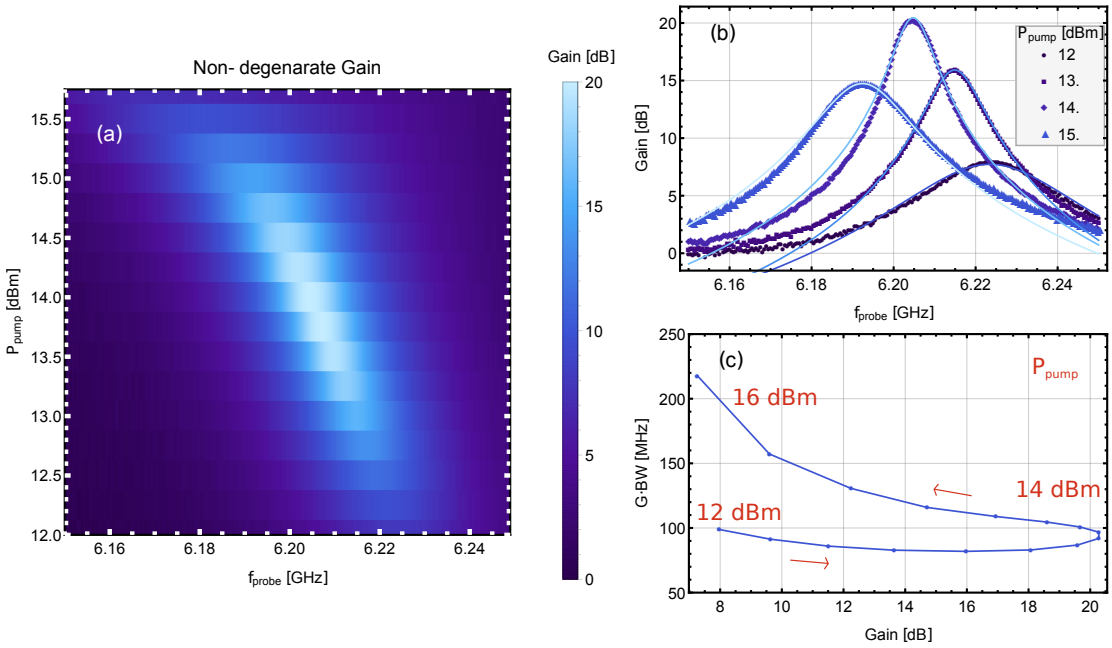

Figure 3.7: Characterizing the JPD in non-degenerate mode as a function of pump power. (a) The JPD gain as a function of the pump power when operated in non-degenerate mode. (b) Selected traces from (a) are fit to obtain the gain-bandwidth-product. (c) The gain-bandwidth product is plotted as a function of gain for several pump powers (red text). At high powers, the gain starts to decrease, while the gain-bandwidth product begins to increase.

$V = -800\,\mathrm{mV}$ appears to be $\omega_{\mathrm{pump}} = 2\pi \cdot 6.7\,\mathrm{GHz}$, to obtain gains in the range of $10 - 20\,\mathrm{dB}$, a substantial pump power must be applied. This pump power shifts the JPD resonances away from the pump frequency [16], and therefore the lower resonance shifts downward. This is clearly seen in figure 3.7 (a) and (b), where the JPD resonance is seen to be around $\omega_{\mathrm{signal}} \approx 2\pi \cdot 6.2\,\mathrm{GHz}$. At $12 \leq P_{\mathrm{pump}} \leq 15\,\mathrm{dBm}$ of input pump power, the JPD gives gain between $5 - 20\,\mathrm{dB}$. Figure 3.7 (c) shows how one crucial amplifier characteristic, the gain-bandwidth product (GBWP) changes as the gain is increased. The GBWP is important when weighing the trade-off between gain and bandwidth; for our purposes, the bandwidth of the amplification chain need only be on the order of the qubit linewidth Γ. Furthermore, we would need a gain high enough to reduce the effect of added noise by subsequent amplifiers in the detection chain.

Once the JPD set-point is chosen with the above procedure, the pump tone is canceled as in [16] (see figure 3.2) by splitting the pump and sending one line through a variable attenuator and phase shifter at room temperature, and then recombining via the directional coupler connecting the JPD to the pump line in the cryostat. The attenuation and phase is tuned manually [17] to minimize the measured signal output at the pump frequency. With this technique, we reduced the measured signal at output 2 at the pump frequency by $\approx 35\,\mathrm{dB}$, which, in conjunction with the combined $80\,\mathrm{dB}$ of isolation of the pump from the sample by the four circulators and isolators, ensures that the strong pump tone does not significantly leak into the wQED sample.

Beyond the gain and the bandwidth of the JPD, it is also important to know the 1 dB compression point and the added noise of the amplification chain. The dynamic range of Josephson parametric amplifiers has been studied in detail in [18]. The 1 dB compression point $P_{1\,\mathrm{dB}}$ of a JPD decreases rapidly when increasing the gain [18]. If the amplifier is compressed, that is, it deviates from its linear behavior, its noise characteristics would differ between measurements of $\Gamma^{(1,2)}(\tau)$ and $H^{(1,2)}(\tau)$, thereby invalidating the noise moment subtraction scheme outlined in chapter 2. An amplifier with too much added noise is similarly counterproductive, in that a lower signal to noise ratio necessitates more averaging to obtain the desired uncertainty in $g^{(2)}(\tau)$ in the exponential scaling discussed above. Figure 3.8 shows the characterization of the JPD working point used for experiments measuring photon correlations outlined in chapter 4.4. The parameters for this set-point are $V_{\mathrm{Coil}} = -753\,\mathrm{mV}$, $\omega_{\mathrm{pump}}/2\pi = 6.38\,\mathrm{GHz}$, and $P_{\mathrm{pump}} = 13.55\,\mathrm{dBm}$. This set the gain of the JPD to $\approx 18\,\mathrm{dB}$ with a bandwidth of 13.6 MHz. The gain was limited from above to ensure a high $P_{1\,\mathrm{dB}}$ comparable to values in [15], and from below to achieve minimize added noise. The value of $P_{1\,\mathrm{dB}}$ was determined by applying and measuring a tone on the JPD signal resonance and varying the tone's power, and comparing this to the measured power of the tone when the JPD pump was off. Thus, at each power we obtain a gain for the JPD, and the tone power at which the gain has decreased by 1 dB gives the compression point. In figure 3.8 (b), the dashed horizontal line marks the gain at which the amplifier has compressed by 1 dB. Note that the horizontal axis is calibrated via fitting the resonance fluorescence of the atom, relating the measured Rabi rate Ω to P_{sample} via equation (2.10). The vertical line shows the power at which the curve intersects this dashed line, giving $P_{1\,\mathrm{dB}} = -109\,\mathrm{dBm} \approx 2750$ photons $\mu\mathrm{s}^{-1}$ for photons in the amplification band. The power from the qubit with linewidth $\Gamma = 2.7\,\mathrm{MHz} \approx 0.1\%$ of $P_{1\,\mathrm{dB}}$. Parts (c) and (d) of figure 3.8 compare the PSD of the measurement line after applying a drive tone with the JPD on and with the JPD off. In the plot, one clearly sees an increased noise level when the JPD is off. Further, part (d) gives the number of noise photons as 2.89 when using the JPD, as compared to 118 noise photons when only the HEMT is used. One also notes that the HEMT amplifier at the output of the JPD is far from ideal operation, with a noise temperature $T_{\mathrm{noise}} \approx 35\,\mathrm{K}$, about an order of magnitude higher than nominal operation of the HEMT. Although T_{noise} as quoted is the noise of amplification chain, the added noise before the HEMT is expected to only be fewer than 10 photons, suggesting that the HEMT adds still $\simeq 100$ noise photons, double the $5\,\mathrm{K} \simeq 55$ photons it should nominally add. Thus, the JPD clearly improves the noise temperature substantially, although the HEMT performance is also sub-optimal.

With careful understanding and calibration of each component in the experimental setup, the cryostat, quantum signal analyzer, and quantum-limited amplifier enable the efficient measurement of the nonclassical light emitted by our artificial atoms. The next chapter details the resulting first- and second-order correlations of the light emitted by a qubit in 1-D open space.

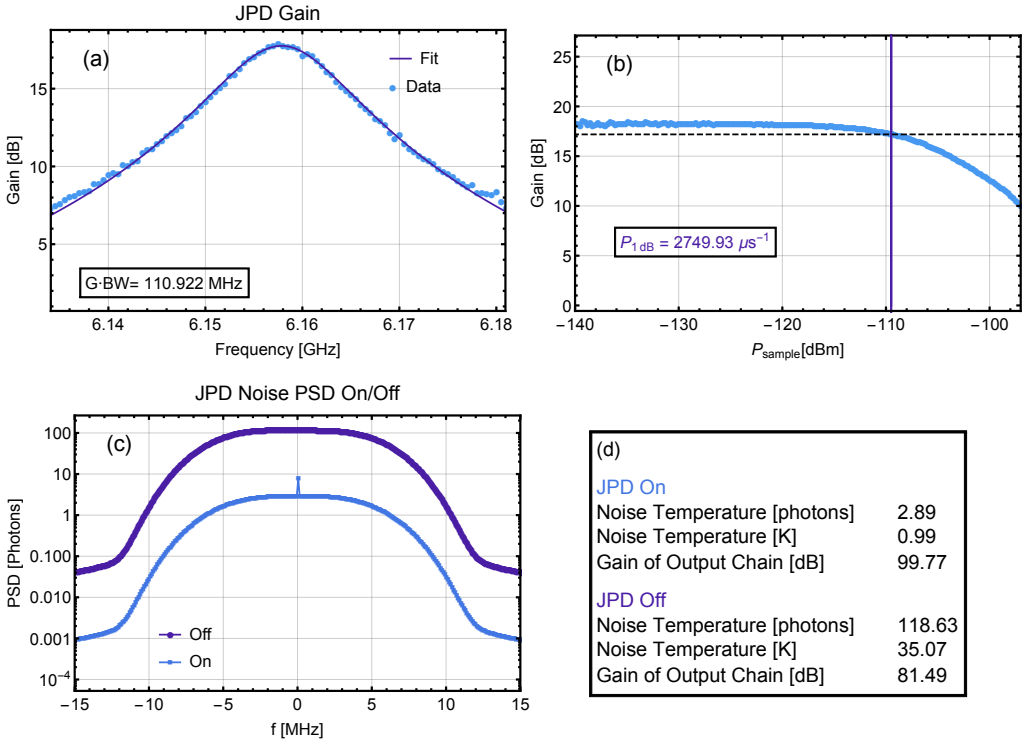

Figure 3.8: Characterization of the JPD for the experiment detailed in chapter 4.4. (a) The gain of the JPD was set to $\approx 18\,\mathrm{dB}$, with a bandwidth of $13.6\,\mathrm{MHz}$. (b) the $1\,\mathrm{dB}$ compression point for the JPD is determined to be $2750\,\mu\mathrm{s}^{-1}$. (c) Power spectral density of the detection line with and without the JPD. The coherent signal is substantially amplified above the noise when the JPD is operating. (d) Comparison of the noise and gain of the output line with and without the JPD on.

Chapter 4

Measurements of nonclassical light in wQED

The experimental setup given in the last chapter described the cryogenics, signal processing, and amplification techniques relevant to the experimental determination of nonclassical correlations of light in wQED. In this chapter, I detail the measurements made which are relevant to understanding a single emitter of nonclassical light. First, spectroscopy of a single qubit is discussed, followed by resonance fluorescence for experiments using two and three transmon levels. Then, intensity correlations of a single qubit are investigated, both with and without the incorporation of a Josephson Parametric Dimer amplifier.

4.1 Spectroscopy of the waveguide QED sample

The first measurement to make is spectroscopy, measuring purely coherent response of the system. This allows us to determine a) the resonance frequencies and the coupling of the qubits to the waveguide and b) the tunability of the transmons with externally applied magnetic field. The magnetic field is supplied by two superconducting coils mounted below the chip, which is seen in figure 3.2 and described theoretically in equation (1.8). The resonance frequency of each transmon is found by a dip in transmittance

$$|t(f)|^2 = |\frac{V_{2,\text{out}}(f)}{V_{1,\text{in}}(f)}|^2. \tag{4.1}$$

Figure 4.1 shows transmittance spectroscopy as a function of voltage in a single coil (the other held fixed). This shows qualitatively the $|\cos(\Phi)|$ behavior of the two transmons' g-e transition, detailed in section 1.3.1, with the magnetic flux through the SQuID $\Phi = M \cdot I_{\text{coil}} + \Phi_{\text{env}}$, coupled via mutual inductance M to the current in the coil I_{coil}. The flux offset Φ_{env} is introduced by the environment, for example due to trapped magnetic flux during the course of the cool-down. To enhance visibility, the data are plotted in arbitrary units, and the median frequency trace taken across all coil voltages was divided from the data, to remove the background spectrum present in measurement line.

The coil voltage was set to $V_{\text{coil}} = -0.187\,\text{V}$, giving the fundamental resonance ω_{ge} of one the lower transmon $\omega_{ge}/2\pi \approx 6.16\,\text{GHz}$, and the higher-frequency transmon tuned to $\omega_{ge}/2\pi \approx 7.36\,\text{GHz}$; the higher-frequency transmon is ignored in the following discussion. To characterize the transmon radiative and non-radiative decay channels, the transmittance around the lower resonance was measured with varying power. The transmittance at arbitrary power and detuning, and in the presence of environmental effects including non-radiative qubit damping Γ_{nr} and pure dephasing Γ_ϕ, is determined by equation (2.19) (see also equation (2.22)). Here I will provide a bit of intuition for what we expect. For a resonator, the spectral shape would be a Lorentzian, independent of the applied power. But qubits, being nonlinear systems, have scattering properties which depend on the power, and thus a power sweep elucidates the nonlinear nature of the qubit. In particular, at low powers the qubit behaves like a nearly-coherent scatterer, and so we expect almost complete extinction. At high powers, the qubit $|e\rangle$-state population is saturated, leaving it unable to accept further excitations. Thus, transmittance increases toward unity, as seen in the inset of figure 4.2. These data were normalized by dividing all signals by the maximum measured signal at the largest power, as the qubit resonance is no longer visible at high powers owing to the equal population of the $|g\rangle$ and $|e\rangle$ states. As given in chapter 4.1, spectroscopy enables us to determine the qubit resonance f_0, decay linewidth Γ_0, and the ratio $\eta = \Gamma_0/(\Gamma_0 + \Gamma_{\text{nr}})$ of the radiative to non-radiative decay linewidths. For the resonance in figure 4.2, we find $\Gamma_0/2\pi = 1.8(6)\,\text{MHz}$, $\Gamma_\phi/2\pi = 0.5(4)\,\text{MHz}$,and $\eta = 0.97$, indicating the qubit is coupled most strongly to the waveguide. Note, however, that thermal excitation due to non-negligible bath temperatures would affect the transmittance curve similarly as pure dephasing and non-radiative decay. A finite bath temperature means that there is always some population of the $|e\rangle$ state. Thus, there will always be some transmittance, as the transmon cannot completely coherently reflect the signal tone. To distinguish pure dephasing from thermal excitation, one could drive the e-f transition, and the transmission dip measured would indicate the population of the $|e\rangle$ state. The three traces shown were fit simultaneously to $|t|^2 = |1 - r|^2$, with r given in (2.22), with all shared parameters except the Rabi rate Ω, whose with applied power in equation (2.10) is taken into account. The fitted Rabi rates are quoted in terms of the radiative linewidth Γ_0, given theoretically by (2.11) in the legend of the plot.

The inset of figure 4.2 shows how the transmittance on resonance changes with applied sample power. Here we can see a minimal transmittance of $|t|^2_{\text{min}} \sim 0.15$. When equation (2.22) includes thermal excitation, this minimum corresponds to a maximum temperature of $\sim 130\,\text{mK}$. This minimum depends on the base temperature achieved in the cryostat, which for this measurement was $\gtrsim 45\,\text{mK}$. Although other cool-downs achieve $|t|^2_{\text{min}} \sim 0.01$, this data was chosen because it is consistent with the cryogenic temperatures for the later experiments.

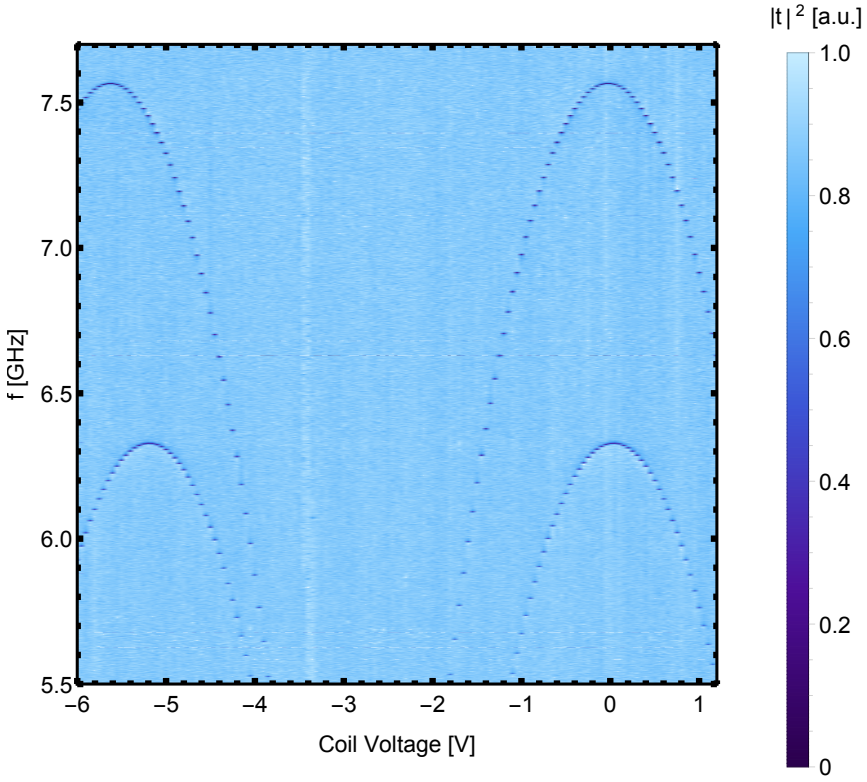

Figure 4.1: Transmittance of wQED sample as a function of coil voltage. The fundamental transmon resonance can thus be adjusted to the needs of the experiment.

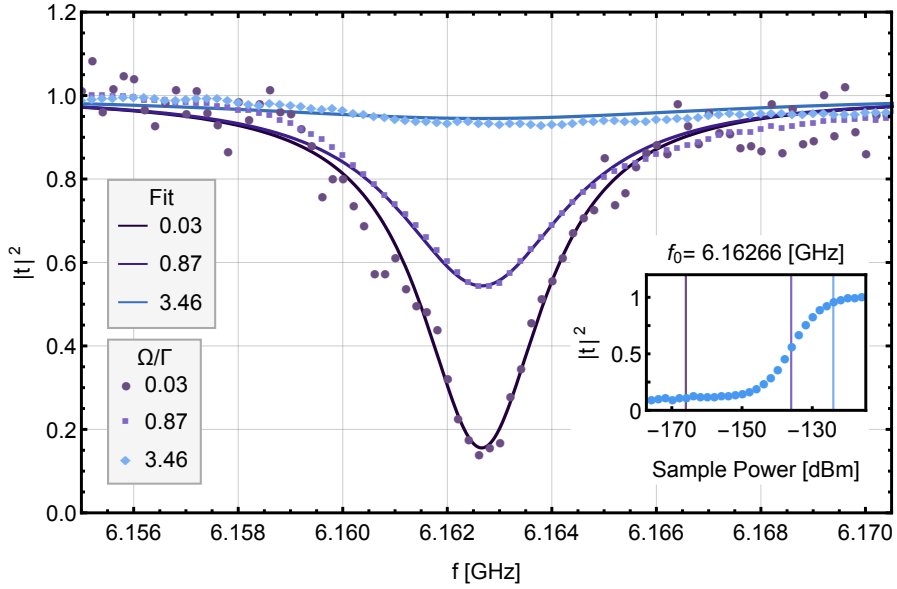

Figure 4.2: Transmittance spectroscopy of one qubit for different drive powers. Inset: the transmittance on resonance $f_0 = 6.16\,\mathrm{GHz}$ as a function of drive power, with the three powers shown in the main plot marked with a vertical line of the same color as the trace.

4.2 Qubit power spectral density

The power spectral density of light emitted by an artificial or natural atom coupled to open space gives properties of the atom such as the linewidth Γ of the addressed transition and, at strong coherent drive powers, the Rabi rate Ω describing coherent oscillations of a single excitation between the field and the atom, forming the dressed states characterized by the Mollow triplet in measurement. The power spectral density for a qubit in a waveguide has been measured in circuit QED [3, 20, 41]. Here I demonstrate our capability of performing resonance fluorescence measurements using the experimental setup described in the previous chapter.

After finding the g-e transition of the transmon with spectroscopy to be $\omega_{ge}/2\pi = 6.1627\,\text{GHz}$, we recorded the auto-correlation of the output signal with the coherent drive on, $G^{(1)}[\tau]$, and off, $H^{(1)}[\tau]$, at the qubit frequency $\omega_d = \omega_{ge}$, while varying the input power of the drive tone. The power spectral density (PSD) is then obtained by taking the Fourier transform of $G^{(1)}[\tau]$, as described in section 2.4.2 and in more detail in appendix B.1. By fitting the resulting Mollow triplets observed from the resonance fluorescence in the PSD to equation 2.32, we are able to map the input power to the power at the sample. In other words, we measure the attenuation of the input line from the generator to the sample. This enables us to know precisely how we vary the drive power at the qubit, and from this, to determine the gain of the amplification chain. Figure 4.3 shows the measured Mollow triplets for several different powers, with the y-axis in photons/s/Hz (equivalently, photons), with the photon power known after determining the gain and attenuation of the measurement lines. For clarity, the single-point peak present from the coherent tone is removed from the data. Furthermore, the JPD was not used in this experiment due to its narrow bandwidth.

The analysis of these data is carried out in several steps. First, the attenuation was determined by fitting the data to the resonance fluorescence equation (2.32) with a free parameter as an overall factor (i.e. fitting to $A \cdot \mathcal{S}(\omega - \omega_d)$, with A as the scaling factor free parameter), as we don't yet know the signal power at the sample. With an input power of $P_{\text{in}} = -44.5\,\text{dBm}$, we found a Rabi rate of $\Omega/2\pi = 11.06\,\text{MHz}$, corresponding to the power at the sample of $P_{\text{sample}} = -118.5\,\text{dBm}$, giving a line attenuation of $\simeq 77\,\text{dB}$. The triplet was measured for both input lines from the same output line, which gave comparable attenuations within 1 dB of each other, validating the symmetric design of the input lines. With P_{sample} determined, we take the measured $G^{(1)}[\tau]$ signal at the FPGA (converted from "clean-sweep units" described in section 3.2 to Watts) and obtain the overall gain of the amplification chain $g = P_{\text{out}}/P_{\text{in}}$. The gain of the output line 1 used in this experiment, shown in figure 3.2, was $g \simeq 90\,\text{dB}$, which includes the warm amplifier board depicted in figure 3.3. After we have the power that the atom emits before the ampilfier, we convert this to photon flux $\phi_\gamma \equiv P/(\hbar\omega_d)$, yielding photons in power spectral density. A summary of how to rescale power into photons/s is given in appendix B.3. The traces were fit simultaneously, with the scaling of Ω with input power,

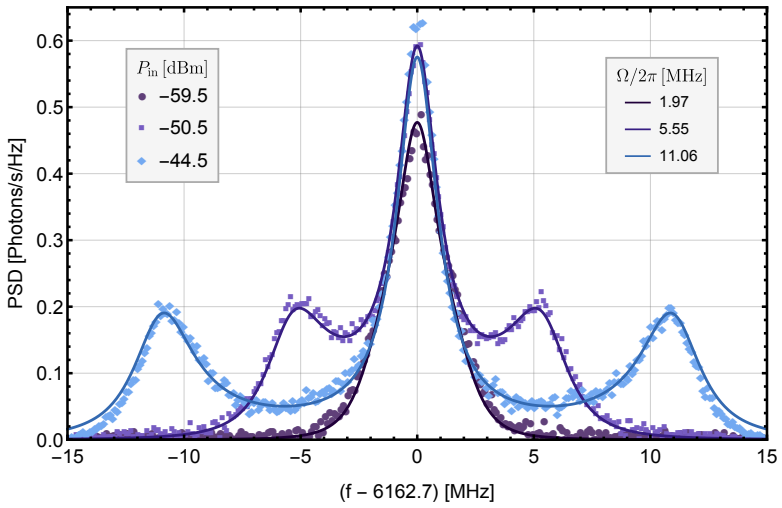

Figure 4.3: Mollow Triplets obtained by strongly driving the lower-frequency transmon in the wQED sample. These data both demonstrate the dressed-state behavior of a strongly driven two-level system and relate the power from the microwave generator to the power seen by the qubit.

given by equation (2.10), included such that only the a single parameter for the power was necessary for the fit. The triplets measured in figure 4.3 give $\Gamma/2\pi = 2.04\,\text{MHz}$, in agreement within the fit error of the damping rate, denoted Γ_0 in the transmon transmittance fits outlined in the previous section. The Rabi rates indicated in the legend. Comparing the two legends one sees that, as the input power is quadrupled (approximately by adding 6 dB of power), the Rabi rate Ω is doubled, in agreement with equation 2.10.

4.3 Power spectral density for a two-photon drive

We further explored the power spectral density of the transmon while driving the transition from the ground state to the second excited state via its two-photon transition, $\omega_{gf/2}$, as shown in figure 2.3. In this experiment, we placed the transmon g-e transition at $\omega_{ge}/2\pi = 5.58\,\text{GHz}$. To find the e-f transition, I then performed performed two-tone spectroscopy, continuously driving the g-e transtition and sweeping a probe tone. With this, the e-f transition was found at $\omega_{ef}/2\pi = 5.2181\,\text{GHz}$, giving an anharmonicity $\alpha/2\pi \simeq -365\,\text{MHz}$. As described in section 2.4.3, the two-photon drive was then set to $\omega_d = \omega_{gf}/2$, chosen at $\omega_d/2\pi = 5.39705\,\text{GHz} \simeq (\omega_{ge} + \alpha/2)/2\pi$. This drive was applied to input 1 of the measurement setup (see figure 3.2) and the power spectral density of the output signal at frequencies around the g-e and e-f frequency were recorded without the JPD, once more for bandwidth reasons. These data are shown in the left column of figure 4.4. To compare to the theory, drive powers Ω, g-e linewidth Γ, and the gain of the amplification chain were determined as described in section 4.2; that is, by measuring and fitting the Mollow triplet of the standard resonance fluorescence type. This measurement determined $\Gamma/2\pi \simeq 1.38\,\text{MHz}$, the input line attenuation to be 76 dB, and the gain to be 85 dB. The linewidth is sensibly lower than previous measurements, as ω_{ge} is lower than g-e transition in the previous section, thereby decreasing the

coupling (see equation (2.11)), but the discrepancy is larger than what could be explained by the difference in resonance. This could be due to a non-flat density of states in the waveguide. The coupling would be substantially lower, for example, if there are weak standing waves due to small impedance mismatches in the line, whose wavelength is off-resonant from the g-e transition at this frequency. Similar analysis is described in prior research in wQED [42]. As predicted in section 2.4.3, the splitting of the g-e and e-f transitions is observed with increasing two-photon drive power. With these fitted parameters, the corresponding theory for the g-e and e-f transition is shown in the right column of figure 4.4. Note that the color-bar of figure 4.4, which is expressed in photons at the frequency of the drive, is shared for all plots.

There are some notable differences between the predictions and measurement. First, the measured power spectral density is lower than predicted, and is it distributed more evenly between the Autler-Townes doublet peaks than predicted. Second, the largest scattering amplitudes appear at higher input powers than predicted. Third, the shift of the peaks appears to be much more rapid with power. There are some adjustments which could be considered in the model presented in section 2.4.3. For example, the factor of $\sqrt{2}$ in the coupling Γ_1 of the e-f level to the field is only true to first order [23]. Similarly to the discrepancy in decay rate Γ with frequency, a non-constant density of states in the waveguide would also lead to different couplings as the frequency changes due to increased drive power [42].

4.4 Photon correlations

The measurement of photon correlations of an artificial atom in 1-D open space, first done in [20], showed superbunching in transmission and antibunching in reflection. The goal of the wQED experiment in Qudev is to measure these for two qubits in a waveguide, using our sample as shown in figure 3.4. Toward this goal, I present intensity correlations of the lower-frequency qubit in the sample. Unlike [20], and similar to [15], we use a single output line, with one experiment using a JPD as the first amplifier in the output line, allowing for efficient measurements of $g^{(2)}(\tau)$ from a single output port, and another using the HEMT as the first amplifier, for comparison.

The experiment is designed to measure $g^{(2)}(\tau)$ for the qubit in both reflection and transmission, and consequently to observe antibunching in the former and superbunching in the latter, consistent with [20]. This would validate the experimental setup to measure the photon statistics for coupled qubits in the waveguide. Recall from chapter 2 that the four measurements needed to measure $g^{(2)}[\tau]$ are $\Gamma^{(2)}[\tau]$, $H^{(2)}[\tau]$, $\Gamma^{(1)}[\tau]$, and $H^{(1)}[\tau]$. These four measurements were interleaved, before averaging, on the FPGA in the quantum signal analyzer, to ensure the noise background for each measurement is as similar as possible, as this is the assumption used to arrive at the subtraction scheme, equation 2.44. Because of the scaling of the number of averages to achieve the same margin of error for the second order as compared to the first order

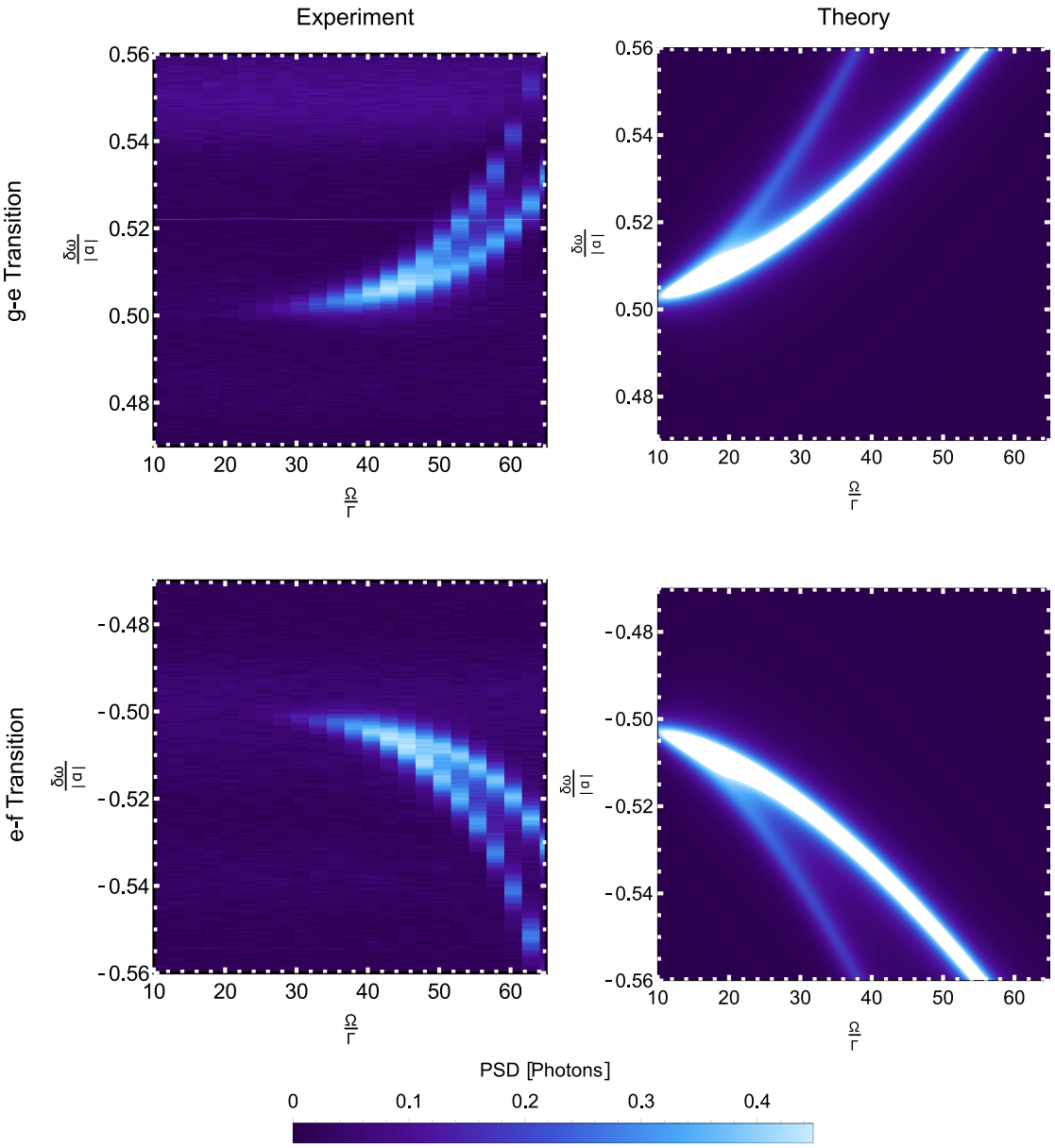

Figure 4.4: Power spectral density measurements of the g-e (top row) and e-f (bottom row) transition under strong two-photon drive $\omega_d = \omega_{gf}/2$. The experiment (left column) and theory (right column) are compared.

traces [11], the second order traces are averaged 16 times for every trace of the first-order measurements. These four measurements are then averaged in blocks, and each block is repeated overnight.

Although the first order correlations are processed as described in the earlier sections, the second order correlations have additional noise considerations. First, we follow previous works [15, 27] which subtract the mean large-τ correlations, such that the mean value of $g^{(2)}[\tau \to \infty] = 1$. Additionally, previous works account for a thermal background state [15, 27] in the $H^{(1,2)}$ measurements for $g^{(2)}[\tau]$. To treat this, the moments of a thermal distribution with photon flux ϕ_γ are subtracted from the measurements with no applied signal $H^{(1,2)}$. In other words, for the subtraction scheme outlined in equation (2.44), the "off" measurements in the original experiment $H^{(1,2)}$ are the "on" measurements in the subtraction scheme, while the thermal correlations are the "off" measurements in the subtraction scheme. The thermal correlations are obtained by generating the time-resolved moments of a thermal field by performing a $g^{(2)}[\tau]$ measurement on the JPD resonance, as the JPD essentially produces thermal light, where the pump is off in the $H^{(1)}[\tau]$, $H^{(2)}[\tau]$ measurements. Knowing the properties of thermal light statistics, we can write, as outlined in section 2.5.1:

$$\begin{aligned} G^{(2)}_{\text{th}}(\tau) &= \left\langle a^\dagger_{\text{th}}(t) a^\dagger_{\text{th}}(t+\tau) a_{\text{th}}(t) a_{\text{th}}(t+\tau) \right\rangle \\ &= \langle \phi_\gamma \rangle^2 \, g^{(2)}_{\text{th}}(\tau) \qquad (4.2) \\ G^{(1)}_{\text{th}}(\tau) &= \langle \phi_\gamma \rangle \, g^{(1)}_{\text{th}}(\tau), \qquad (4.3) \\ & \qquad (4.4) \end{aligned}$$

where $\phi_\gamma = \langle n_{\text{th}} \rangle$ is the mean power of the thermal field, in photon flux (see appendix B.3). Because we want to compare our measurements with vacuum, not a thermal state, we subtract from the $H^{(1,2)}$ measurements in the original experiment the thermal correlations obtained by the JPD, scaled by the free parameter ϕ_γ, obtaining a new "off measurement $H^{(1,2)\prime}[\tau]$. We perform the subtraction scheme of the original "on" data with $H^{(1,2)\prime}[\tau]$ as the new "off" data. This then gives the properly normalized statistics, including the thermal state present in the system. The thermal photon flux ϕ_γ was set as free parameter, which is determined by finding the smallest value which yields physically meaningful, positive $g^{(2)}[\tau]$ for the trace with the lowest signal-to-noise ratio, and for our experiments is $\phi_\gamma = 0.18\,\mu\text{s}^{-1}$ at the photon frequency, about three times as high as those measured for previous work [15]. Interpreting this photon flux as a thermal field, one can determine the number of thermal photons per mode in the detection bandwidth by dividing by the bandwidth BW $\sim 10\,\text{MHz}$. This gives $\langle n_{\text{th}} \rangle \sim .018$ photons, corresponding to a bath temperature of $T_{\text{bath}} \approx 73\,\text{mK}$. This is surely hotter than the base temperature of the fridge, but is in agreement with the minimum transmittance measured in 4.2, which gives a maximum bath temperature of $T_{\text{bath}} \lesssim 130\,\text{mK}$. This is sensible, as the base temperature is the minimum temperature that the

system could be in; the components which connect the sample to the room-temperature electronics contribute an additional heat load. The data without this correction are presented in appendix E.

Aside from residual thermal states, one also considers the finite detection bandwidth and its influence on $g^{(2)}[\tau]$ measurements. In general, this is computationally expensive, although one work showed that one can take this detection bandwidth into account via master equation simulations with two "detector" two-level systems in the master equation with bandwidth and frequency of the detection, as in [12]. However, in the high-noise, low-signal limit, this is approximated via two convolutions of the $g^{(2)}[\tau]$ data with the squared filter kernel, as was performed in [26]. The filter kernel used in the experiments was a Chebyshev filter with a bandwidth of $\simeq 10\,\mathrm{MHz}$ and a running-average "boxcar" filter. This is the narrowest boxcar filter described in appendix D. Incorporating this filtering using the small-SNR limit as in [26] gives comparable results for $g^{(2)}[\tau]$ as in [15], simply "leveling" the signal height slightly, bringing it toward $g^{(2)}[\tau] \to 1$ (see [26]). The reflection predictions included a superposition of the qubit signal with a 4% reflectance of the coherent tone by the sample, as we had seen this fraction of the coherent power reflected in the experiment.

With the general considerations of photon correlation measurements outlined, I now detail the experiments in order of complexity. I will first discuss a measurement of $g^{(2)}[\tau]$ using a commercial HEMT as the first amplifier instead of the JPD. Then, I will present the same experiment in which the JPD is used, offering a comparison of measurements incorporating the JPD under otherwise similar experimental conditions.

4.4.1 Measurement without the Josephson Parametric Amplifier

Intensity correlations were measured for the lower-frequency transmon at frequency $\omega_{ge}/2\pi = 6.2052\,\mathrm{GHz}$, with the second transmon similarly detuned as in section 4.1. The signal was recorded from output 1 of the measurement setup in figure 3.2, which had gain of $g \simeq 86\,\mathrm{dB}$ and a noise power spectral density of 60 photons of the amplification chain. The applied power $P_{\mathrm{sample}} \sim -138\,\mathrm{dBm}$ was chosen because it was expected to give a Rabi rate to line-width ratio $\Omega/\Gamma \simeq \sqrt{2}/2$, which theoretically displays antibunching in reflection and superbunching in transmission. The measurements were performed over 40 measurement blocks with 16 million averages per block, resulting in a total of ~ 670 million averages. The data agree well with theory in power spectral density, as shown in figure 4.5, for both reflection and transmission. The signal-to-noise ratio is $SNR \simeq 0.003$, determined by comparing the noise photons from the HEMT and the PSD amplitude seen in figure 4.5. This provides a reference for comparison to the SNR when using the JPD, discussed later.

The intensity correlations shown in figure 4.6 display qualitative agreement

with theory. As described above, the data take into account $\phi_\gamma = 0.18\,\mu s^{-1}$ of thermal photon flux. The theoretical predictions in figure 4.6 (c) and (d) were calculated as in 2.34; given the master equation and the quantum regression formula, one can determine the steady-state intensity correlations of the field. The most notable difference between theory and experiment is the reflection measurement quickly rises as $\tau \to 0$. This is speculated to be an effect from filtering with a low signal-to-noise, as outlined in appendix D. The data before $\sim 100\,\text{ns}$ appear to have artifacts similar to measurements in appendix D with small SNR. Although this appears to be an artifact of filtering, this is not explained in theory by filter convolutions discussed in the previous section. These artifacts rather have the temporal shape similar to the Chebyshev filter, but why this is the case at short times is not well understood, but is also measured in $g^{(2)}[\tau]$ for coherent states in appendix D. Aside from this, the data share the same features with the theory, with the transmission measurement obtaining reaching similar values at zero time, both of which are above 2, suggesting superbunching. In reflection, the greatest similarity to data was achieved when the phase of the reflected tone in the model was set to 0. At this phase, both the data and the theory have a minimum value near $\tau \lesssim 100\,\text{ns}$, and a rise as $\tau \to 0$.

4.4.2 Measurement with the Josephson Parametric Amplifier

In an effort to reduce the necessary averaging while still using a single measurement output line, the $g^{(2)}[\tau]$ measurement is performed with a JPD (described in section 3.4)as the first amplifier. In this experiment, the same qubit is tuned to the JPD frequency which had the desired compression point, gain, and bandwidth (see section 3.4), such that $\omega_{ge}/2\pi = 6.15775\,\text{GHz}$. This frequency is sufficiently similar to the previous experiment to make them comparable, though it is not identical because the prior experiment discussed was not restricted to the JPD frequency constraints. The four measurements are averaged on the FPGA in blocks of 8 million, and repeated overnight. These are then averaged together to yield, for this experiment, 64 million averages. The noise temperature of the amplification chain with the JPD on, given in figure 3.8, is 2.89 photons, corresponding to a minimum SNR of $SNR \sim 0.08$ at the input power comparable to the data in the previous experiment without the JPD. As discussed in appendix C, this means that with the JPD, one would need to take ~ 1000 times fewer averages with the JPD, than without, to obtain the same accuracy of $g^{(2)}[\tau]$. Thus, the $g^{(2)}(\tau)$ measurements presented in the last section would, in principle, need to be repeated 100-fold to obtain the accuracy of this measurement.

For the $g^{(2)}[\tau]$ measurements described here, the JPD bandwidth limits the detectable frequencies (see figure3.8), and so the resulting spectrum is the atom resonance fluorescence (2.32), filtered by the Lorentzian lineshape of the JPD shown in 3.8 (a). These data are fit to the resonance fluorescence equation (2.32), multiplied by the fit JPD Lorentzian with bandwidth $\Gamma_{\text{JPD}} \simeq 13\,\text{MHz}$ (see figure 3.8 (a)), and are shown in figure 4.7, with PSD both in re-

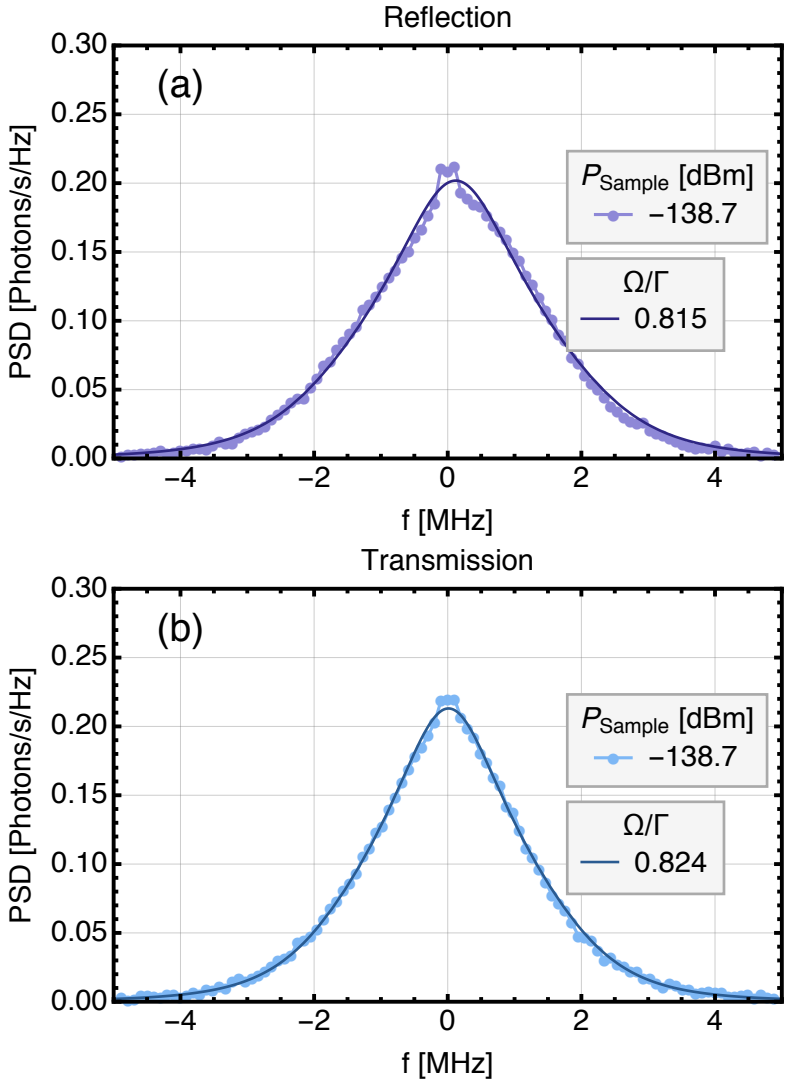

Figure 4.5: Resonance fluorescence $\mathcal{S}[f]$ obtained in the experimental setup for measuring $g^{(2)}[\tau]$ without a JPD. The detuning f is relative to the transmon resonance $\omega_{ge}/2\pi$. Legends indicate the input power to the sample and the corresponding fit to Rabi rate Ω, in units of the linewidth Γ.

flection and transmission. The frequency f is relative to the qubit resonance, which is $\omega_{ge}/2\pi \simeq 6.15775\,\text{GHz}$. Similar to figure 4.3, the fits held constant all parameters except the applied power, which is expressed in terms of Rabi rate via equation (2.10), normalized by the transmon linewidth, found to be $\Gamma/2\pi \approx 1.83(2)\,\text{MHz}$. This is again smaller than we would expect if it were due only to the lower resonance frequency than the previous experiment. This could once more be due to a non-constant density of states in the waveguide, which couples to the transmon more weakly at this resonance.

The set of Rabi rates explored here are small, and therefore we do not see the "shoulders" of the triplet forming, However, we do see that as drive power increases, so too does the incoherently scattered light. The data at these low Rabi rates are comparable for both reflection and transmission. However, the scaling of the Rabi rate with power seems to deviate from theory. The fit suggests that the scaling with power is smaller than predicted, because the amplitude

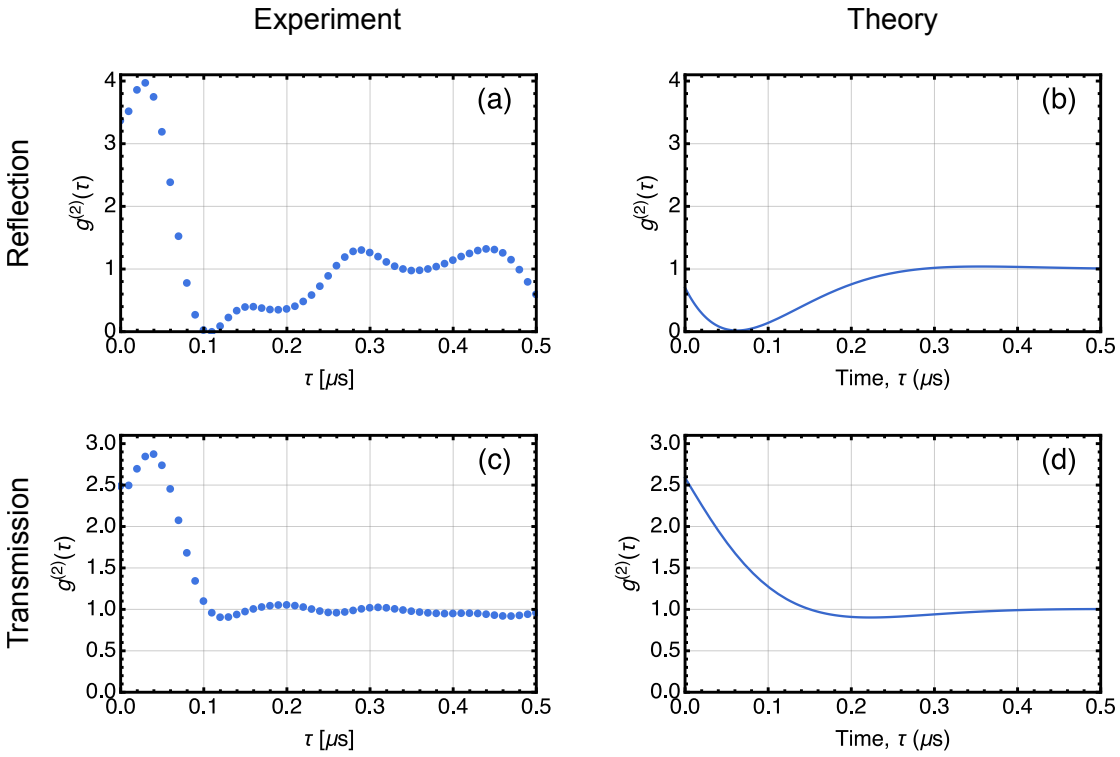

Figure 4.6: $g^{(2)}(\tau)$ for a single qubit with the HEMT as the first amplifier. Comparison of theory and experiment, in reflection and transmission.

difference between traces in theory is larger than in data. This could suggest amplifier compression, as the stronger drive tones resonant with the qubit are incident on the JPD. As the 1 dB compression point for the JPD at this set-point $P_{1\,\mathrm{dB}} = -109\,\mathrm{dBm}$ was $\sim 20\,\mathrm{dB}$ larger than largest coherent drive power $P_{\mathrm{coh,max}} = -130\,\mathrm{dBm}$ applied to the sample, we had expected the amplifier to be linear. Prior work has measured $g^{(2)}[\tau]$ with powers at this fraction of the compression point incident on a JPD [15]. However, it was discovered that the JPD coil, which in part determines its amplification characteristics, was resistively coupled to the electrical ground of the cryostat. Thus, the stability of the JPD set-point depended on the stability of the cryostat ground. It is possible therefore that the 1 dB compression point of the amplifier deviated from the originally set value. Note also that if one relaxes the scaling requirements, the fit function describes these curves well, suggesting the scaling with power is what has changed, and not other factors.

Including the first order correlations just discussed, we take the $\Gamma^{(2)}[\tau]$, $H^{(2)}[\tau]$ data and calculate $g^{(2)}[\tau]$ for the single qubit. The measured $g^{(2)}[\tau]$ from measuring a qubit in the wQED sample is shown in figure 4.8. As in [26], the long-time mean offset of the data due to amplifier noise is subtracted from the data. Furthermore, as in [27, 15], a residual thermal photon flux $\phi_\gamma = 0.18\,\mu\mathrm{s}^{-1}$ is taken into account, which would cause our $g^{(2)}[\tau]$ values to be otherwise nonphysical.

The $g^{(2)}[\tau]$ data are shown in figure 4.8 (a) and (c) in reflection and transmis-

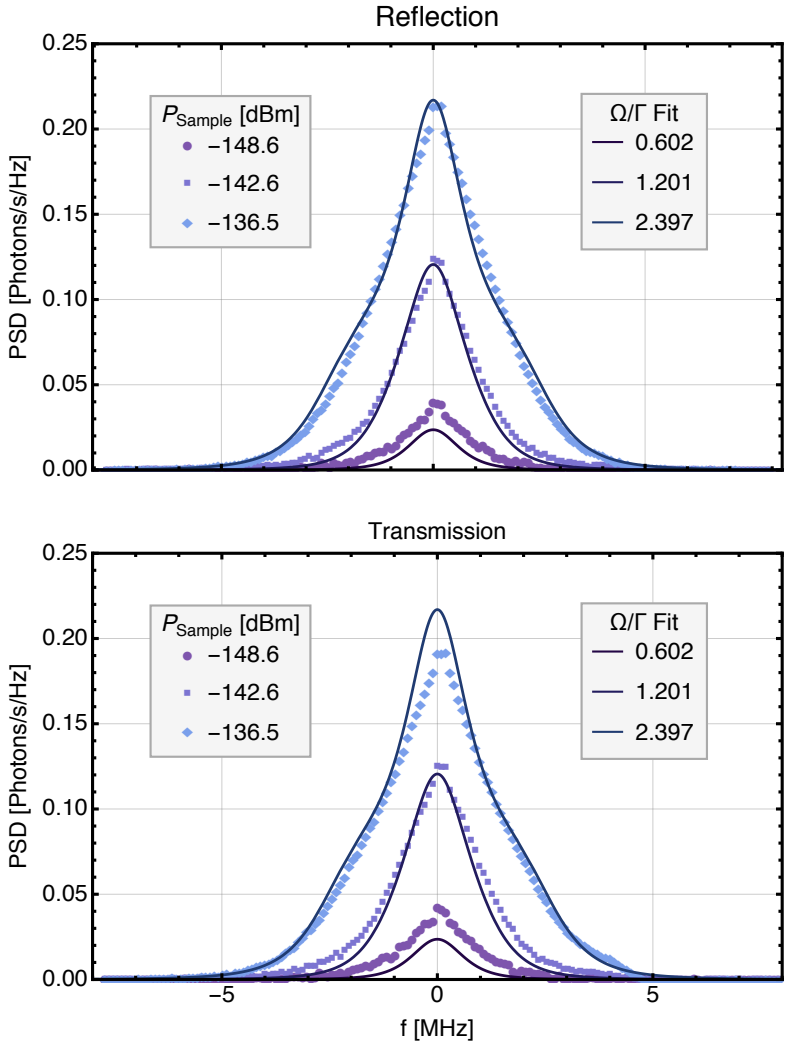

Figure 4.7: Resonance fluorescence $\mathcal{S}[f]$ obtained in the experimental setup for measuring $g^{(2)}[\tau]$. The detuning f is relative to the transmon resonance in the experiment. The JPD limits the detection bandwidth, accounted for in the fitting routine. Legends indicate the input power to the sample and the corresponding fit to Rabi rate Ω, in units of the linewidth Γ.

sion, respectively. In reflection, one sees a clear trend of antibunching, with all traces at $g^{(2)}[0] \sim 0.5$. The presence of oscillations in the data increase with decreasing Rabi rate. This seems to propose a signal-to-noise dependence, as the scattered power for the most weakly driven measurement is $\sim 1/5$ that of the most strongly driven measurement. Comparing to the theory in figure 4.8 (b), we see a qualitative similarity with the data. There is a bump above $g^{(2)} \sim 1$ for the most strongly driven measurement, and the two more weakly driven measurements follow a similar trend as in the theory, although the weakest data trace has, again, more oscillations. Although the phase of the signal is unknown, in figure 4.8 (b), it was found that the phase of the reflected tone which best matched the measurements was π. This is inconsistent with the previous experiment, although this phase could also be dependent on the qubit frequency, accounting for this discrepancy.

The transmission data in figure 4.8 (c) have fewer oscillations than the reflec-

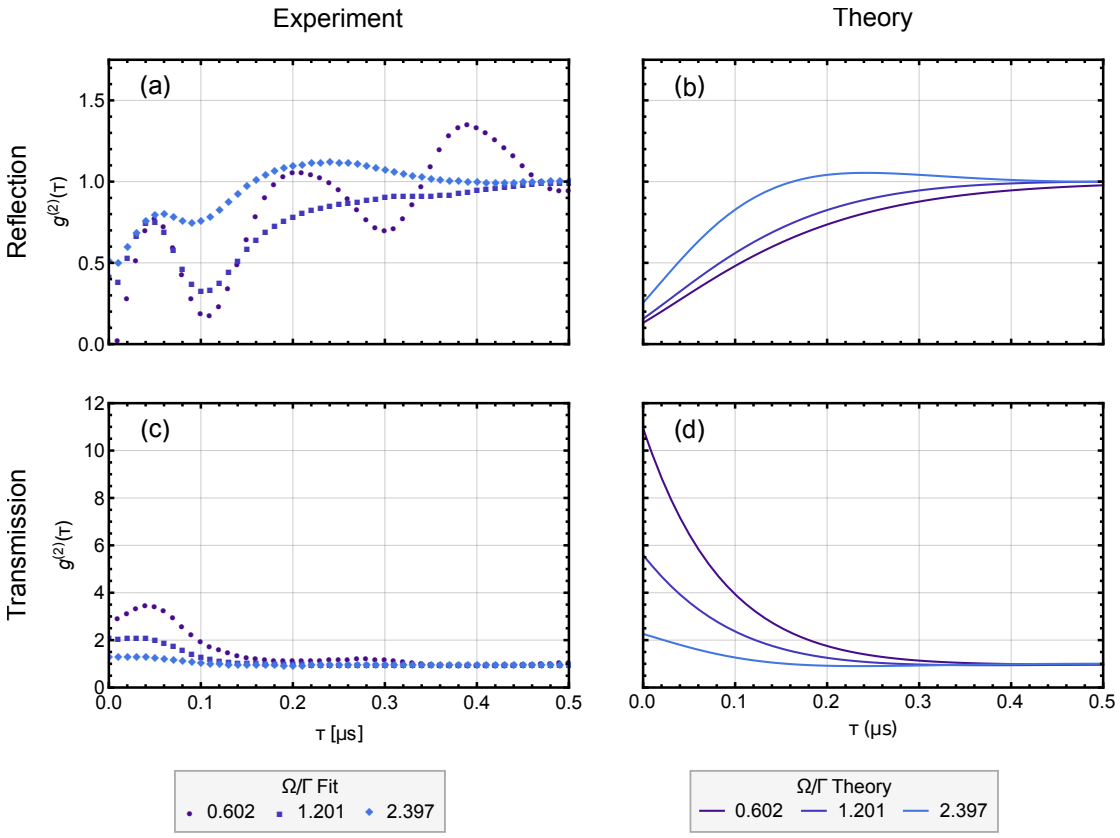

Figure 4.8: $g^{(2)}(\tau)$ for a single qubit. Comparison of theory and experiment, in reflection and transmission.

tion data, and at low powers superbunching is seen. The magnitude of superbunching predicted in figure 4.8 (d) is not measured, though this is could again be due to filter effects which obfuscate the short-time-delay signals (see appendix D); the effects of the FIR filter can be seen at the first peak and trough of the reflection data, as this is also seen in the coherent $g^{(2)}[\tau]$ measurements outlined in appendix D.

Why reflection data have much more oscillations than transmission data is an interesting question, for both measurements scatter the same power, which means if the SNR were the cause, then similar oscillations would be expected for both cases. If there is some sort of assymetry in how the noise interacts with superpoissonian and sub-poissonian light, this would explain the difference.

4.5 Discussion

The experiments experiments presented here span three levels of measurement complexity in waveguide QED. The single-qubit spectroscopy and resonance fluorescence experiments in sections 4.1, 4.2 are well-understood and allow both for characterization of the transmons and for calibration of the input and output lines of the system. Knowing the power at the sample with the Mollow triplet measurements, one can then monitor the gain of the amplification chain and address gain stability and noise performance issues therein. A stable

gain and low noise temperature are critical to measurements of higher-order correlation functions, for the level and stability of the added noise is imperative for the subtraction scheme in equation (2.44). Thus, the resonance fluorescence presents itself as a valuable diagnostic tool for waveguide QED experiments.

The two-photon drive experiment showed a similar power-dependence on the g-e and e-f transitions as we predicted, but to obtain strong quantitative agreement would require a reassessment of the model. Further experiments to probe the $g - f/2$ transition, which was predicted in section 2.4.3 to show a Mollow triplet-like energy splitting, would provide more information about the discrepancies between the data and the theory.

The $g^{(2)}[\tau]$ measurements for a single qubit show a qualitative resemblance to the theoretical predictions, but other effects are perturbing the system which are not accounted for. Nevertheless, we are able to see superbunching in transmission and antibunching in reflection, which shows the quantum nature of the single qubit that we are measuring, comparable to prior work [20]. Further investigation into the cause of the oscillations in our measurements, especially at low powers, is ongoing. As seen in appendix D, the signal-to-noise ratio seriously influences the physical meaningfulness of the data. Although in principle, noise that is uncorrelated with the source and has zero mean should be removed with the subtraction scheme in equation 2.44, even slight amplifier compression would lead to noise that is correlated with the signal, invalidating the subtraction scheme used to calculate $g^{(2)}[\tau]$.

The stability of the JPD is also something which must be carefully monitored. Though care was taken to ensure the $P_{1\mathrm{dB}}$ of the JPD was comparable to previous successful $g^{(2)}[\tau]$ measurements in [15], the discovered coupling of the JPD coil may have caused the set-point to shift, reducing its compression point.

Even with a stable amplification setup, we would like to examine the compression points of the amplifiers at each stage in the chain to know precisely at which powers the amplified noise could change. Although the JPD has the lowest 1-dB compresson point, an experiment examining the behavior of $g^{(2)}[\tau]$ as a function of $P/P_{1\,\mathrm{dB}}$ for a coherent state of power P with only the HEMTs in place would provide insight about what input powers to the HEMTs start to cause a change in the on/off noise characteristics. This same experiment, performed in D, was done with the JPD in place, but a confirming experiment with the JPD would also be valuable, now that we are certain that the JPD set-point is isolated from other DC lines.

Additionally, transmons in the waveguide geometry are subject to a wider bandwidth of spectrally flat (white) noise, unlike transmons surrounded by a cavity with detuned resonance, which filters their electromagnetic environment. While prior work had shown comparable results [20] in $g^{(2)}[\tau]$ measurements, one notable difference between our experiments and those in [20] is that we did not measure extinction below $|t|^2 \simeq 0.2$ in the presented set of measurements, which could be indicative of thermal noise populating the qubit. Investigating the thermal environment and how this could influence the

excited-state population of the transmon will continue to be explored. This can be done, for example, by adding additional attenuation at base temperature. Though it is not clear if this is needed, as in our current setup, the base-temperature Nyquist noise should be domanant (see section 3.1). Improving thermalization of the sample (simply by ensuring strong mechanical contact between objects meant to be of the same temperature) and thermalizing the HEMT amplifiers, will positively influence the signal quality.

Measuring the zero-time correlation functions by measuring the moments of the field via histogramming is another potential avenue for observing correlations between multiple transmons at different detunings, or different levels of the same transmon. This would provide less information than the time-resolved case, but can be used to cross-reference the time-resolve measurements and possibly estimate ϕ_γ by deconvolving the moments of the thermal field in the histogram [14].

On the three-level dynamics front, measuring photon cross-correlations of the two transitions would also be an interesting pursuit on the path to multi-transition correlation measurements. Additionally, we have considered that one can use the $e - f$ fluorescence as a measure of the thermal population of the transmons, which would provide further information regarding sources of noise degrading the signal quality of $g^{(2)}[\tau]$ measurements to date. It may also be worth exploring this as a way to measure the thermal photon flux ϕ_γ. Further research into cascaded photon correlations which also is amenable to the theory in [12] would be a promising avenue to explore pumping the atom with a drive non-resonant to the detection, which would decouple the drive and measurement frequencies.

4.6 Outlook

Waveguide QED holds potential for advancements in the investigation of atoms interacting via a continuum of electromagenetic one-dimensional modes, captivating the minds of theorists and experimentalists alike. Long-term applications of waveguide QED include the study of long-range interactions between atoms mediated by photons, as well as medium-range interactions, where the time delay between atoms is comparable to the decay time of the atoms [19]. The prospect of routing single photons in a 1-D waveguide has also been studied [36, 37], with on-chip single-photon sources readily available [33]. Additionally, one can explore a non-constant, engineered density of states of a waveguide with an emitter resonant near a photonic bandgap [29]. Combining the advanced methods of photon correlation functions with the rich body of interactions achievable in waveguide QED will bring about new insights into fundamental quantum optics and open an avenue for characterizing Hamiltonians engineerable only by freeing the atoms from their electromagnetic cages.

Appendix A

Theoretical clarifications

A.1 Flux quantization and the SQuID Loop

This section outlines some of the details which lead to flux quantization, and the phase-flux relationships which emerge in SQuID geometries. This section is essentially an abridged description from Richard Feynman's *Lectures on Physics, Vol. III*, chapter 21.

Due to the gauge-invariance of quantum mechanics, the phase φ of the wavefunction of a charged particle $\psi = |\psi|e^{i\varphi}$ as the particle moves from point a to point b along path $\boldsymbol{s}$ in a magnetic field $\boldsymbol{B} = \boldsymbol{\nabla} \times \boldsymbol{A}$ is changed by the vector potential $\boldsymbol{A}$ according to

$$\Delta\varphi = \frac{q}{\hbar}\int_a^b \boldsymbol{A} \cdot d\boldsymbol{s}.$$

One then can extend the Schrödinger equation to include this vector potential and solve for the probability current density, which, for a superconductor, is indeed the charge current density. By considering the current density inside a superconducting ring to be $\boldsymbol{J} = 0$ on account of the Meissner effect, one can then show the phase of the superconducting wavefunction

$$\hbar\nabla\phi = 2e\boldsymbol{A}.$$

By taking a line integral around a closed loop inside the superconducting ring, one finds

$$\hbar \oint \boldsymbol{\nabla}\phi \cdot d\boldsymbol{s} = \frac{2e}{\hbar}\Phi,$$

where Φ is the magnetic flux through the loop $\boldsymbol{s}$, and is thus the flux through the non-superconducting part of the ring, as there is no flux inside the superconductor itself. Thus, we can relate the phase of the superconducting state to the applied magnetic field. But we can go one step further. Note that the wavefunction must have the same value at the same point, therefore we have the requirement that $\theta_b - \theta_a = 2\pi n$ for integer n, and because

$$\theta_b - \theta_a = \hbar \oint \boldsymbol{\nabla}\phi \cdot d\boldsymbol{s}$$

we see

$$2\pi n\hbar = 2e\Phi \Rightarrow \Phi_0 = \frac{h}{2e} \tag{A.1}$$

requires the magnetic flux be discrete in units of the flux quantum Φ_0.

Let's extend this to two junctions in a loop, so the current has two paths a and b with which it can flow from one end of the loop to the other. The total current through the loop that we measure is $I_{\text{tot}} = I_a + I_b$. The phase drop across the paths a and b is

$$\Delta\varphi_a = \varphi_{a0} + \frac{2e}{\hbar}\int_{\text{a}} \boldsymbol{A}\cdot d\boldsymbol{s}_a$$
$$\Delta\varphi_b = \varphi_{b0} + \frac{2e}{\hbar}\int_{\text{b}} \boldsymbol{A}\cdot d\boldsymbol{s}_b$$

and should be equal, since the total phase drop must be the same. Taking the difference of the inital phases of each path, we see

$$\begin{aligned}\varphi_{b0} - \varphi_{a0} &= \frac{2e}{\hbar}\int_{\text{b}-\text{a}} \boldsymbol{A}\cdot d\boldsymbol{s}_{b-a} \\ &= \frac{2e}{\hbar}\Phi\end{aligned}$$

If we consider the phase to have offset φ_0, then the total current through the junction then is obtained via the Josephson relations (1.3):

$$\begin{aligned}I_{\text{tot}} = I_a + I_b &= I_c\left(\sin(\varphi_0 - \frac{2e}{\hbar}\Phi) + \sin(\varphi_0 + \frac{2e}{\hbar}\Phi)\right) \\ &= 2I_c\sin(\varphi_0)\cos(\frac{2e}{\hbar}\Phi)\end{aligned}$$

Now it is difficult to control what φ_0 is in practice, but its contribution to the total current is bounded by $\sin(\varphi_0) \leq 1$, so we have

$$I_{\text{max}} = 2I_c\left|\cos(\frac{2e}{\hbar}\Phi)\right| \tag{A.2}$$

Thus, the SQuID behaves like a Josephson junction, with a tunable critical current.

A.2 The rotating frame

The dynamics of a quantum system are invariant under unitary transformations, which boils down to the claim that physics is invariant under basis transformations. Quantum mechanically, we can show this by considering the Schrödinger equation in a basis containing $|\psi\rangle$:

$$\partial_t|\psi\rangle = \frac{-i}{\hbar}H|\psi\rangle \tag{A.3}$$

Given an operator A, the propagator is a unitary operator $U = e^{-iAt/\hbar}$. We can define a different state $|\tilde{\psi}(t)\rangle \equiv U^\dagger(t)\,|\psi\rangle$. If $|\tilde{\psi}(t)\rangle$ is a valid quantum state, it too satisfies the Schrödinger equation. The Hamiltonian $\tilde{H}$ which satisfies this can be solved for as:

$$\begin{aligned}
\tilde{H}\,|\tilde{\psi}\rangle &= i\hbar\partial_t\,|\tilde{\psi}\rangle \\
i\hbar\partial_t\,|\tilde{\psi}\rangle &= i\hbar\partial_t U^\dagger(t)\,|\psi\rangle \\
&= U^\dagger(t) i\hbar\partial_t\,|\psi\rangle + i\hbar\dot{U}^\dagger(t)\,|\psi\rangle \\
&= U^\dagger(t) H\,|\psi\rangle - AU^\dagger(t)\,|\psi\rangle \\
&= \left(U^\dagger(t) H U(t) - A)U^\dagger(t)\right)|\psi\rangle \\
\tilde{H} &= U^\dagger(t) H U(t) + i\hbar\dot{U}(t)U^\dagger(t)
\end{aligned} \tag{A.4}$$

So, to transform H into a rotating frome, we need only apply equation A.4, which provides the transformations omitted in chapter 2 when considering dynamics in the frame of the drive. Further approximations are made after entering the rotating frame, however, where fast-rotating terms are ignored because, at the time-scales measured in experiment, these oscillations average to zero. For information about the rotating wave approximation, see [25] and references therein.

Appendix B

Signal processing

B.1 Power spectral density with discrete signals

The most important relation to know for these experiments exploring correlations and frequency spectra is the Wiener-Khinchine Theorem. The continuous case states that the power spectral density $\mathcal{S}(f)$ is derived from the amplitude autocorrelation $\langle S^*(0) S(\tau)\rangle$ by

$$\begin{aligned} \mathcal{S}(f) &= \mathcal{F}\{\langle S^*(0) S(\tau)\rangle\} \\ \mathcal{S}(f) &= \int_{-\infty}^{\infty} \langle S^*(0) S(\tau)\rangle e^{2\pi i f\tau} \,\mathrm{d}\tau \end{aligned} \tag{B.1}$$

where $\mathcal{F}\{\cdot\}$ denotes the continuous Fourier transform. Note that the units of $\mathcal{S}(f)$ are $[\langle S^*(0) S(\tau)\rangle] \cdot s = [\langle S^*(0) S(\tau)\rangle]$ /Hz, as expected for a power spectral density (e.g. V^2_{rms}/Hz). The Virtex 4, however, delivers only discrete signals $S[\tau]$ of length $N_s = 1024$ points, with time spacing $\Delta\tau = 10\,\mathrm{ns}$. The Wiener-Khinchine Theorem in the discrete case is then straightforward:

$$\begin{aligned} \mathcal{S}[f_k] &= \mathcal{F}[\langle S^*[0] S[\tau]\rangle]\,\Delta\tau \\ \mathcal{S}[f_k] &= \sum_{j=1}^{N_s} \langle S^*[0] S[\tau_j]\rangle e^{2\pi i f_k \tau_j} \Delta\tau \\ &= \sum_{j=1}^{N_s} \langle S^*[0] S[(j-1)\Delta\tau]\rangle e^{2\pi i (k-1)(j-1)/N_s} \Delta\tau \end{aligned} \tag{B.2}$$

where here $\mathcal{F}[\cdot]$ denotes the discrete Fourier transform, and we used the notation $\tau_j \equiv (j-1)\Delta\tau$ and $f_k \equiv \frac{k-1}{N_s \Delta\tau}$. Thus, to obtain the physically meaningful power spectral density from a digitized signal, one need only take the (unnormalized) discrete Fourier transform and multiply by the time bin resolution $\Delta\tau$.

Note that the clock speed of the FPGA determines the sampling rate (here 100 MHz, corresponding to 10 μs). This means that the maximum frequency one can measure (called the *Nyquist* frequency) is 50 MHz. Any signals above the Nyquist frequency are *folded* into the band below the Nyquist frequency, an artifact also known also as *aliasing*. For this reason, we have in place an anti-aliasing analog low-pass filter at the input of the ADC (see figure 3.3.

B.2 Determining the gain of the amplification chain

The gain of the amplification chain is given by

$$P_{\text{FPGA}} = gP_{\text{sample}} \tag{B.3}$$

In reality, the gain g is an effective gain, consisting of attenuators and amplifiers. Nevertheless, this allows us to rescale all measured quantities to quantities at the sample.

To know the attenuation of the input line, we fit the Mollow triplet formed by driving the qubit with a strong coherent drive (see chapter 4.2). Determining the gain then is found by

$$P_{\text{FPGA}} = gAP_{\text{input}}, \tag{B.4}$$

where A is the attenuation in the input line. Thus, all power spectral density measurements can be converted to Watts/Hz at the sample, by determining the gain and attenuation of the output and inputs to the sample. This provides a measurement of thermal noise in the system, including noise added by amplifiers, which enables us to evaluate and characterize the noise properties of the amplifiers, quantum-limited or otherwise.

B.3 Converting to quantum-friendly units

While units like voltages are typical in standard laboratory settings, it is most understandable and physically relevant to measure power in terms of *photon flux* ϕ_γ, that is

$$\phi_\gamma = \frac{P_{\text{signal}}}{\hbar\omega},$$

where $\hbar\omega$ is the photon energy of the emitter. Note the unit of ϕ_γ is $[\phi_\gamma] = \text{s}^{-1} = \text{Hz}$, and can intuitively be understood as the frequency of photons that pass by our detection.

There are a few considerations in making this transformation in practice. Let's start again where we measure-at the FPGA. After the signal is emitted from the sample, it undergoes several stages of (unintentional) attenuation and amplification. Provided that the amplifiers and attenuators are all linear, we know that the FPGA signal S_{FPGA} and the signal right out of the sample S_{sample} are proportional to one another:

$$S_{\text{FPGA}} = \sqrt{g}S_{\text{sample}}, \tag{B.5}$$

where here g is the total gain of the amplification chain, including the attenuation η in the signal output line $g = \eta g_{\text{ideal}}$.

So by compensating for the gain in the amplification chain, we can determine

$$P_{\text{sample}} = \frac{\left\langle S^*_{\text{sample}} S_{\text{sample}} \right\rangle}{2Z},$$

where the numerator has units of $V_{0-\text{pk}}$, and Z is the impedance of the signal line. Thus, measuring the power at the sample in terms of number of photons (in s^{-1}) is

$$\phi_{\gamma,\text{sample}} = \frac{\left\langle S^*_{\text{sample}} S_{\text{sample}} \right\rangle}{2Z\hbar\omega}.$$

Finally, substituting our expression of S_{sample} in terms of what we measure via equation (B.5), we have:

$$\phi_{\gamma,\text{sample}} = \frac{\left\langle S^*_{\text{FPGA}} S_{\text{FPGA}} \right\rangle}{2Z\hbar\omega g} \tag{B.6}$$

One should also note that I've left out the time-dependence of the signals processed here; this is because this technique applies to both pure intensity measurements $\left\langle S^*_{\text{FPGA}} S_{\text{FPGA}} \right\rangle [\tau]$ and amplitude-correlation measurements $\left\langle S^*_{\text{FPGA}} [0]\, S_{\text{FPGA}} [\tau] \right\rangle$. It really amounts to dimensional analysis, but the interpretation of the two mentioned quantities is of course different.

B.4 Determining noise temperature of the output line

The previous section discussed how to convert measured signals into "quantum-friendly" units, namely describing the light in terms of photons. When measuring power spectral density, there is a flat noise floor in the measured amplitudes due to thermal Nyquist noise in the lines. For any given frequency whose power spectrum is from purely thermal origins, the expected number of photons follows Bose-Einstein statistics:

$$\langle n_{\text{th}} \rangle = \frac{1}{e^{\hbar\omega/k_{\text{B}}T} - 1} \tag{B.7}$$

As we know that the power spectral density is measured in photons, knowing the attenuation and the gain of the amplifier, one may simply read the number of noise photons constituting the power spectral density noise floor. Thus, with the gain and the attenuation of the output and input lines respectively, measuring the power spectral density of the noise gives $\langle n_{\text{th}} \rangle$, the expected number of thermal noise photons.

Appendix C

Signal-to-noise ratio and attenuation before the first amplifier

Here I outline a calculation which determines how much added attenuation between the output of the sample and the first amplifier effects the signal-to-noise ratio, demonstrating the added attenuation to the JPD via extra circulators and cabling do not diminish the advantage the JPD offers over measurements with the HEMT as the first amplifier. Provided the first amplifier has sufficient gain, the SNR with the amplifier added noise is the dominant contributor of noise to the signal. I will therefore only consider the SNR at the first amplifier.

Consider a single photon emitted from the transmon. This can in principle be emitted equally in either direction a_{L} or a_{R}, resulting in an output power $P_{\mathrm{out}} = P_{\mathrm{photon}}/2 = \hbar\omega_{ge}\Gamma/2$, or $n_{\mathrm{signal}} = 0.5$ photons. Without loss of generality, but to give some reasonable values, let's assume $\omega_{ge}/2\pi = 6\,\mathrm{GHz}$. At the sample, as described in section 3.1, there are $n_{\mathrm{noise}} \simeq 0.58$ photons at 6 GHz. So the signal-to-noise ratio (SNR), defined as $\mathrm{SNR} \equiv \mathcal{S}_{\mathrm{signal}}/\mathcal{S}_{\mathrm{noise}}$, equivalently the ratio of the number of signal photons to noise photons, is, at the sample $\mathrm{SNR}_{\mathrm{sample}} \simeq 0.86$.

The SNR at the amplifier is given by $\mathrm{SNR}_{\mathrm{amp}} = n_{\mathrm{signal}} \cdot A_{\mathrm{out}}/n_{\mathrm{amp}}$, where A_{out} is the attenuation of the output line between the sample and the amplifier, and n_{amp} is the number of noise photons at the amplifier, plus the added noise by the amplifier.

For output line 1 in figure 3.2, which would go from the sample to the HEMT as the first amplifier, the total attenuation is $A_{\mathrm{out1}} = -5.2\,\mathrm{dB}$, with $-2\,\mathrm{dB}$ from the first output line to the first circulator, a nominal $-1\,\mathrm{dB}$ of total insertion loss for the circulator and isolator, a nominal $-1\,\mathrm{dB}$ for the UT-85-SSSS (stainless-steel for both the inner- and outer-conductor) coaxial cable between the circulator and the isolator, and another $-1.2\,\mathrm{dB}$ insertion loss in the bandpass filter. Furthermore, the 40 mK noise is attenuated by the isolator and bandpass filter by $-1.7\,\mathrm{dB}$, and 100 mK noise is added to the output line at the HEMT input. Assuming the nominal 5 K of added noise photons by the HEMT, the total number of noise photons with these specifications gives $n_{\mathrm{HEMT}} \approx 57$

noise photons, while the $-5.2\,\mathrm{dB}$ of attenuation gives means the signal at the HEMT input is only $n_{\mathrm{signal,HEMT}} \approx 0.15$ photons, giving $\mathrm{SNR}_{\mathrm{HEMT}} \approx 0.003$.

The output line which has a JPD as the first amplifier benefits from the fewer added noise photons by the JPD, but also has additional line attenuation due to the added circulators, which protect the wQED sample from the strong pump tone needed to power the JPD. The attenuation between the sample and the JPD in output line 2 in figure 3.2 is a total of $A_{\mathrm{out2}} = -7\,\mathrm{dB}$. The attenuation per component is $-2\,\mathrm{dB}$ from the line between the sample and the first circulator, $-0.5\,\mathrm{dB}$ from the first circulator, $-2\,\mathrm{dB}$ from the line connecting the first to the second circulator, $-1.5\,\mathrm{dB}$ for the block of three circulators, two of which are used as isolators, and another $-1\,\mathrm{dB}$ from the line connecting the circulators to the directional coupler combined with the insertion loss of the directional coupler.

This attenuation then results in a signal of $n_{\mathrm{signal,JPD}} \approx 0.1$ photons, about 67% of the line to the HEMT. But, the added noise is merely $n_{\mathrm{JPD}} \approx 2.66$ photons, assuming the JPD adds only 1 photon of noise and considering the thermal noise $n_{\mathrm{pump}} \approx 1.66$ photons from the pump lines, which have lesser attenuation than the signal input lines and therefore give a larger number of noise photons than the figures quoted in section 3.1 for the input line thermal noise. Then we obtain $\mathrm{SNR}_{\mathrm{JPD}} \approx 0.037 \approx 14 \cdot \mathrm{SNR}_{\mathrm{HEMT}}$, reducing the noise contribution to the total signal substantially.

The ratio of the noise power for the HEMT line and the JPD line then determines the fraction of how many more repetitions R are needed to obtain the same accuracy in measuring $g^{(2)}[\tau]$. This scales as [11]

$$\begin{aligned} \frac{R_{\mathrm{HEMT}}}{R_{\mathrm{JPD}}} &= \left(\frac{n_{\mathrm{HEMT}}}{n_{\mathrm{JPD}}}\right)^2 \\ &= 463 \end{aligned} \tag{C.1}$$

Thus, if the given $g^{(2)}[\tau]$ measurement with the JPD takes an hour, the equivalent measurement with the JPD would take 19 days to obtain the same SNR. If additionally the different signal power is taken into account by taking $\left(\frac{\mathrm{SNR}_{\mathrm{JPD}}}{\mathrm{SNR}_{\mathrm{HEMT}}}\right)^2$, one would find that the same measurement with the HEMT line would take 8 days. Here we see that, despite the added attenuation from the sample to the JPD, the substantially lower noise temperature at the first amplifier of the line makes the JPD a remarkably more suitable amplifier for quantum signals.

Appendix D

Digital filtering of coherent photon correlations

To understand the signal processing methodologies thoroughly, intensity correlation measurements, as in section 4.4, were performed for coherent light; that is, the qubit was tuned $\sim 500\,\mathrm{MHz}$ out of the measurement band. Then the signal in this experiment $\Gamma^{(2)}[\tau]$ was the coherent tone at frequency $\omega_{\mathrm{coh}}/2\pi = 6.172\,\mathrm{GHz}$, and this was done for four different finite-impulse response (FIR) digital filter settings and four different powers. The JPD was used, with a set-point with 13 dB gain, 19 MHz bandwidth, 1-dB compression point of $9734\,\mu\mathrm{s}^{-1}$, and noise temperature $T_{\mathrm{noise}} = 6.3$ photons. As the bandwidth of the JPD is quite wide, the detection band can be limited by applying different FIR filters. In order from widest to narrowest, the filters are:

1. A Chebyshev filter with a pass-band$\simeq 20\,\mathrm{MHz}$, denoted "Cheb30" by the name given in `CleanSweep`
2. The same Chebyshev filter with an additional moving-average filter
3. A Chebyshev filter with a pass-band$\simeq 10\,\mathrm{MHz}$, denoted "Cheb15"
4. This same "Cheb15" filter, with the added box-car filter

Figure D.1 shows the time-domain weight of the filters which are convolved with the measured data. They have several distinct features. For both Chebyshev filters, applying the boxcar filter reduces the central peak weight and slightly shifts the first dip of the filter. The narrow-band Chebyshev filter also naturally has a longer time-scale. The measured noise PSD gives the transfer function that each filter applies to the signal. Figure D.2 shows the white noise spectrum of the detection band after applying one of the four filters. Figure D.2 shows that filters without the four-point boxcar filter have a residual peak at $-25\,\mathrm{MHz}$. This is due to a DC offset which originates from the imperfect downconversion and digitizing [28], which is shifted by the digital downconversion. The boxcar filter is designed to eliminate signals at this frequency. The different powers of the coherent tones in the measurement were designed to be ones that are comparable for drive tones we would apply to a qubit. Assuming $\Gamma \sim 2\,\mathrm{MHz}$, the powers corresponded to Rabi rates

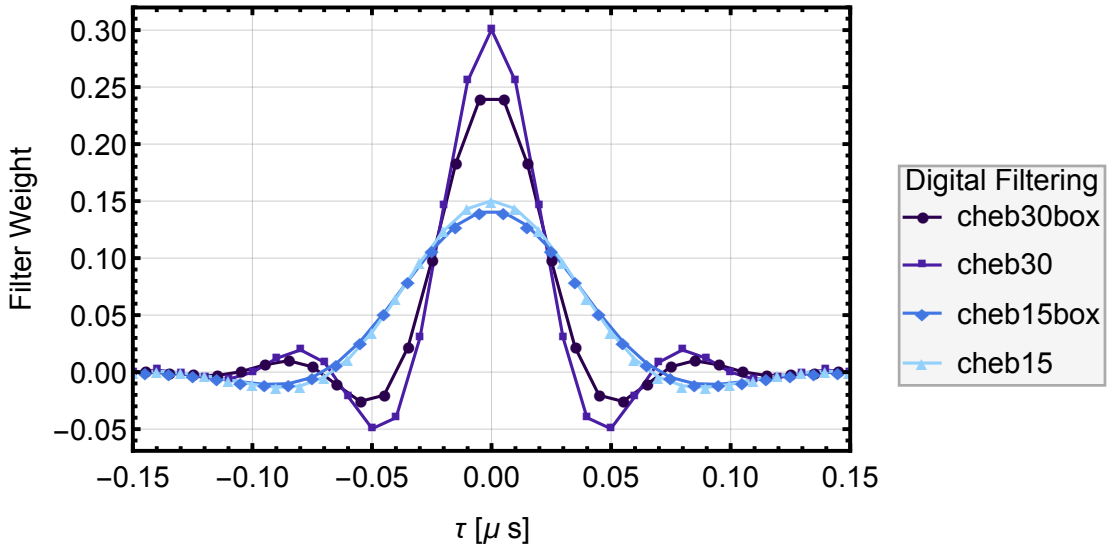

Figure D.1: The FIR filters compared, plotted in the time-domain.

of $\{\Omega\} = \{2\Gamma, \Gamma, \Gamma/2, \Gamma/4\}$. The right-hand column of figure D.3 shows the PSD of each measurement, with each row corresponding to a different power in descending order. This column gives the sense of the SNR of the coherent peak relative to the thermal noise photons in the detection band. From highest to lowest power, the SNR of these data are $\simeq \{39.89, 9.95, 2.43, 0.61\}$, not considering the DC peak as thermal noise.

The $g^{(2)}[\tau]$ data on the left column of figure D.3 shows how the intensity correlations are influenced by filtering when comparing the traces in each plot, and how this influence changes with SNR when comparing traces in different rows. In the top-left plot, we see that $g^{(2)}[\tau]$ is quite coherent, but there are features at $\tau < 200\,\text{ns}$ which deviate from the expected $g^{(2)}[\tau]$ of a coherent tone. Specifically, there is a peak and a dip for all traces in the plot; for the traces which were filtered by the narrow Chebyshev filter, the peak and dip appear at $\tau \sim 50\,\text{ns}$ and $\tau \sim 110\,\text{ns}$, respectively. These correspond to the different time-scales of the filters in figure D.1.

One can see that signal-to-noise ratio (SNR) plays a large role in $g^{(2)}[\tau]$, as the high-power signals (seen by the coherent peak height relative to the noise floor in the noise PSD), converge to the expected value of $g^{(2)}[\tau] = 1$, regardless of filter type. At the lowest powers, unphysical results occur, with $g^{(2)}[0] < 0$ for the widest-band filter. This emphasizes the importance of reducing added noise, as any quantum signal would have a small signal when compared to these high coherent powers, requiring exponentially more repetitions to obtain a $g^{(2)}(\tau)$ which is accurate and physically meaningful.

This experiment shows the artifacts the different filters introduce to applied signals which we understand, with noise levels realistic for experiments. The top-left plot shows that even at high SNR, these filters alter the measured $g^{(2)}[\tau]$. The presence of a DC peak (seen at $-25\,\text{MHz}$) in the PSD at the top right is seen in the $g^{(2)}[\tau]$ top-left plot by 25 MHz oscillations in the $g^{(2)}[\tau]$

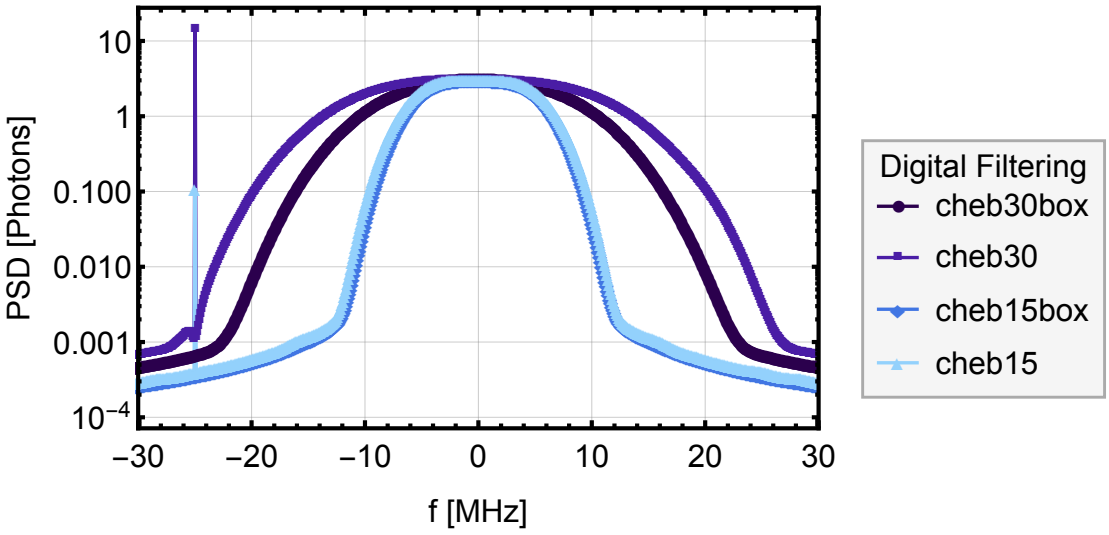

Figure D.2: Noise power spectral density of the outoput signal for each different filter combination. The boxcar filter removes the peak from DC offsets seen here at $-25\,\mathrm{MHz}$ (see text).

wide trace without the boxcar. The scale of these artifacts are small and even at high SNR are non-negligible, but in principle they do not explain the discrepancy with theory that we see when measuring $g^{(2)}[\tau]$ of a transmon.

One important note is that the gain of the amplification chain for each different applied power, at applied power $\Omega/\Gamma = 1/2 \approx 10\,\mu\mathrm{photons\,s^{-1}}$, the gain of the amplification chain drops from 95 dB to 93 dB. This is characteristic of amplifier compression, despite having characterized a high compression point of the JPD prior to this measurement. This could be a result of the observed JPD coil's coupling to ground, and thus the set-point could have shifted over the course of these overnight measurements. Still, even at high powers, where the gain is reduced by several dB, the $g^{(2)}[\tau]$ still shows quite coherent characteristics. The next dataset to obtain would be one with only HEMT amplifiers at the output, as they are simpler to use and hence more reliable in terms of their set-point characteristics, and have a high comression point. What this proposed experiment would show is whether the observed artifacts are due to compression, or not.

Another experiment which would be valuable would be to examine $g^{(2)}[\tau]$ as a function of the power normalized by the $1-$ dB compression point would directly give information about how compression influences $g^{(2)}(\tau)$.

As the dataset stands, we see clearly that the normalization scheme approaches expected values for coherent states, and that we can measure coherent $g^{(2)}[\tau]$ for high SNR, but effects from the filter are still visible. Future experiments like the one described here would shed light on the question of the significance of filtering and compression on the measurable photon statistics. I note that these filter effects are also present in previous work demonstrating photon blockade [26], though at the scale presented there, they are not visible.

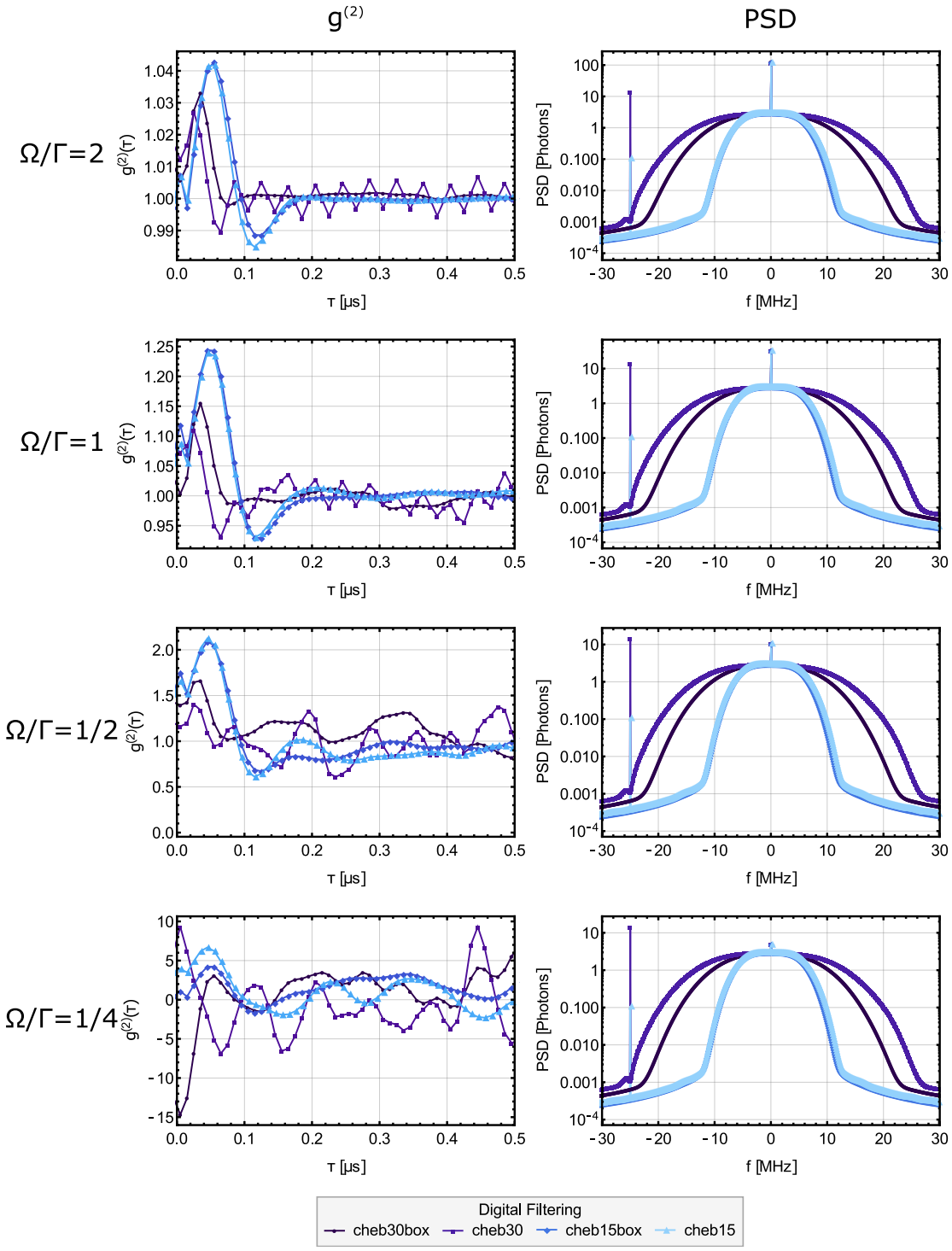

Figure D.3: Comparing $g^{(2)}[\tau]$ for coherent states for different filtering methods at different powers. The left column shows $g^{(2)}(\tau)$, right column shows PSD, with SNR inset. The rows vary the power, with highest on top, and lowest on bottom.

Appendix E

Raw intensity correlation measurements

Here I give the $g^{(2)}[\tau]$ measurements which were presented, but without the correction for a thermal background flux. These data are the "raw" results, performing the subtraction scheme on the measured data. After considering the added thermal field with the scheme described in section 4.4, these data give $g^{(2)}[\tau] > 0$. Without this taken into account, it is possible to calculate $g^{(2)}[\tau] < 0$ in reflection.

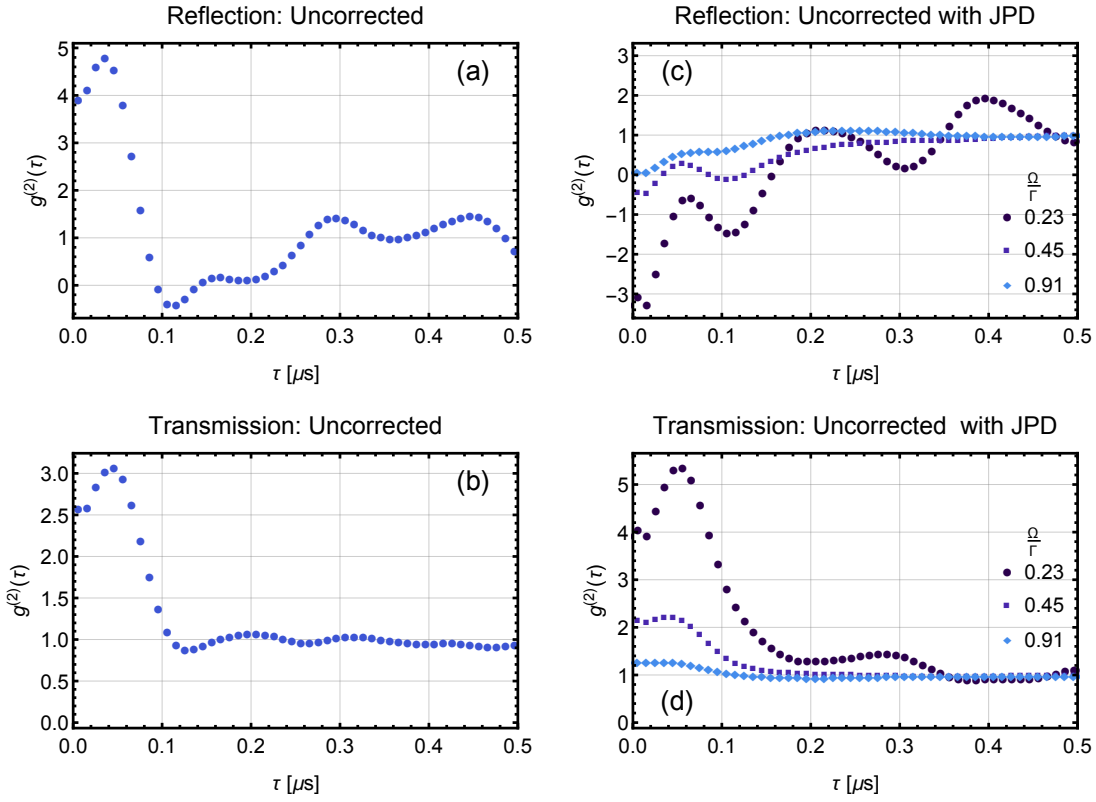

Figure E.1: $g^{(2)}(\tau)$ for a single qubit without correction for a residual thermal photon flux ϕ_γ. Plots (a) and (b) are with the HEMT as the first amplifier in reflection and transmission, respectively. Plots (c) and (d) use the JPD as the first amplifier.

Acknowledgements

First and foremost, it has been a real pleasure working alongside the inquisitive and motivated QuDev group. I cannot thank Prof. Dr. Andreas Wallraff enough for his dedication and exemplary scientific skillset, making this Master's project truly an exciting one. I'd especially like to thank Dr. Simone Gasparinetti for his engagement in and guidance during the project. His broad knowledge base provided exceptional insight into the theory, as well as the experimental and technical details necessary to undertake meaningful research. I am very thankful to have worked with Robin Buijs for the duration of my thesis. His constant willingness to discuss and appreciate new findings with me, and his help in data acquisition, demonstrated what it means to work together toward a common goal. His acute observational skills in experiment proved their value time and time again during this work. Beyond the main waveguide QED team, I'd like to thank Marek Pechal and Michele Collodo for lending their experience and for always being willing to share their wisdom. It's been a pleasure traveling the world together at lunch breaks! Additionally, Dr. Anton Potočnik readily shared his insights of the nuances involved in characterizing a JPD. I am indebted to the group as a whole, for enabling a cooperative, motivating, and friendly place to do science. Beyond the lab, I'm so grateful for the support system I've had here and at home. I thank my girlfriend for all of her support during this part of life which left little time for nice dinners or weekend trips. I'd also like to thank my parents for their unconditional support throughout this transformative time in my scientific career.

Bibliography

[1] A. A. Abdumalikov, O. Astafiev, A. M. Zagoskin, Yu. A. Pashkin, Y. Nakamura, and J. S. Tsai. Electromagnetically induced transparency on a single artificial atom. *Phys. Rev. Lett.*, 104(19):193601, May 2010.

[2] A. A. Abdumalikov, O. V. Astafiev, Yu. A. Pashkin, Y. Nakamura, and J. S. Tsai. Dynamics of coherent and incoherent emission from an artificial atom in a 1d space. *Phys. Rev. Lett.*, 107:043604, Jul 2011.

[3] O. Astafiev, A. M. Zagoskin, A. A. Abdumalikov Jr., Yu. A. Pashkin, T. Yamamoto, K. Inomata, Y. Nakamura, and J. S. Tsai. Resonance fluorescence of a single artificial atom. *Science*, 327(5967):840–843, 2010.

[4] M. Baur, S. Filipp, R. Bianchetti, J. M. Fink, M. Göppl, L. Steffen, P. J. Leek, A. Blais, and A. Wallraff. Measurement of autler-townes and mollow transitions in a strongly driven superconducting qubit. *Phys. Rev. Lett.*, 102(24):243602, June 2009.

[5] V. Bouchiat, D. Vion, P. Joyez, D. Esteve, and M. H. Devoret. Quantum coherence with a single Cooper pair. *Phys. Scr.*, T76:165–170, 1998.

[6] D. Bozyigit, C. Lang, L. Steffen, J. M. Fink, C. Eichler, M. Baur, R. Bianchetti, P. J. Leek, S. Filipp, M. P. da Silva, A. Blais, and A. Wallraff. Antibunching of microwave-frequency photons observed in correlation measurements using linear detectors. *Nat. Phys.*, 7(2):154–158, February 2011.

[7] H. P. Breuer and F. Petruccione. *The theory of open quantum systems*. Oxford University Press, 2002.

[8] H. J. Carmichael. *Statistical Methods in Quantum Optics 1: Master Equations and Fokker-Planck Equations*. Springer-Verlag, Berlin, 2 edition, 2002.

[9] C. M. Caves. Quantum limits on noise in linear amplifiers. *Phys. Rev. D*, 26:1817–1839, 1982.

[10] A. A. Clerk, M. H. Devoret, S. M. Girvin, Florian Marquardt, and R. J. Schoelkopf. Introduction to quantum noise, measurement, and amplification. *Rev. Mod. Phys.*, 82(2):1155–1208, Apr 2010.

[11] Marcus P. da Silva, Deniz Bozyigit, Andreas Wallraff, and Alexandre Blais. Schemes for the observation of photon correlation functions in circuit QED with linear detectors. *Phys. Rev. A*, 82(4):043804–12, Oct 2010.

[12] E. del Valle, A. Gonzalez-Tudela, F. P. Laussy, C. Tejedor, and M. J. Hartmann. Theory of frequency-filtered and time-resolved *n*-photon correlations. *Phys. Rev. Lett.*, 109:183601, Oct 2012.

[13] G. J. Dolan. Offset masks for lift-off photoprocessing. *Applied Physics Letters*, 31(5):337–339, 1977.

[14] C. Eichler, D. Bozyigit, and A. Wallraff. Characterizing quantum microwave radiation and its entanglement with superconducting qubits using linear detectors. *Phys. Rev. A*, 86:032106, Sep 2012.

[15] C. Eichler, J. Mlynek, J. Butscher, P. Kurpiers, K. Hammerer, T. J. Osborne, and A. Wallraff. Exploring interacting quantum many-body systems by experimentally creating continuous matrix product states in superconducting circuits. *Phys. Rev. X*, 5:041044, Dec 2015.

[16] C. Eichler, Y. Salathe, J. Mlynek, S. Schmidt, and A. Wallraff. Quantum-limited amplification and entanglement in coupled nonlinear resonators. *Phys. Rev. Lett.*, 113:110502, Sep 2014.

[17] Christopher Eichler. *Experimental Characterization of Quantum Microwave Radiation and its Entanglement with a Superconducting Qubit*. PhD thesis, ETH Zurich, 01 2013.

[18] Christopher Eichler and Andreas Wallraff. Controlling the dynamic range of a josephson parametric amplifier. *EPJ Quantum Technology*, 1(1):2, 2014.

[19] Yao-Lung L Fang, Huaixiu Zheng, and Harold U Baranger. One-dimensional waveguide coupled to multiple qubits: photon-photon correlations. *EPJ Quantum Technology*, 1:3, 2014.

[20] Io-Chun Hoi, Tauno Palomaki, Joel Lindkvist, Göran Johansson, Per Delsing, and C. M. Wilson. Generation of nonclassical microwave states using an artificial atom in 1D open space. *Phys. Rev. Lett.*, 108(26):263601–, June 2012.

[21] Io-Chun Hoi, C. M. Wilson, Gï¿½?Â¶ran Johansson, Tauno Palomaki, Borja Peropadre, and Per Delsing. Demonstration of a single-photon router in the microwave regime. *Phys. Rev. Lett.*, 107(7):073601–, August 2011.

[22] B. D. Josephson. Possible new effects in superconductive tunnelling. *Physics Letters*, 1(7):251–253, July 1962.

[23] Jens Koch, Terri M. Yu, Jay Gambetta, A. A. Houck, D. I. Schuster, J. Majer, Alexandre Blais, M. H. Devoret, S. M. Girvin, and R. J. Schoelkopf. Charge-insensitive qubit design derived from the Cooper pair box. *Phys. Rev. A*, 76(4):042319, 2007.

[24] K. Koshino, H. Terai, K. Inomata, T. Yamamoto, W. Qiu, Z. Wang, and Y. Nakamura. Observation of the three-state dressed states in circuit quantum electrodynamics. *Phys. Rev. Lett.*, 110(26):263601–, June 2013.

[25] K. Lalumière, B. C. Sanders, A. F. van Loo, A. Fedorov, A. Wallraff, and A. Blais. Input-output theory for waveguide qed with an ensemble of inhomogeneous atoms. *Phys. Rev. A*, 88:043806, Oct 2013.

[26] C. Lang, D. Bozyigit, C. Eichler, L. Steffen, J. M. Fink, A. A. Abdumalikov Jr., M. Baur, S. Filipp, M. P. da Silva, A. Blais, and A. Wallraff. Observation of resonant photon blockade at microwave frequencies using correlation function measurements. *Phys. Rev. Lett.*, 106(24):243601–4, Jun 2011.

[27] C. Lang, C. Eichler, L. Steffen, J. M. Fink, M. J. Woolley, A. Blais, and A. Wallraff. Correlations, indistinguishability and entanglement in Hong-Ou-Mandel experiments at microwave frequencies. *Nat. Phys.*, 9(6):345–348, June 2013.

[28] Christian Lang. *Quantum Microwave Radiation and its Interference Characterized by Correlation Function Measurements in Circuit Quantum Electrodynamics*. PhD thesis, ETH Zurich, 02 2014.

[29] Yanbing Liu and Andrew A. Houck. Quantum electrodynamics near a photonic band-gap. *arXiv:1603.02998 [quant-ph]*, March 2016. arXiv: 1603.02998.

[30] Rodney Loudon. *The Quantum Theory of Light*. Oxford U, 2000.

[31] B. R. Mollow. Power spectrum of light scattered by two-level systems. *Phys. Rev.*, 188:1969–1975, 1969.

[32] Y. Nakamura, Y. A. Pashkin, and J. S. Tsai. Coherent control of macroscopic quantum states in a single-Cooper-pair box. *Nature*, 398(6730):786–788, April 1999.

[33] M. Pechal, L. Huthmacher, C. Eichler, S. Zeytinoğlu, A.?A. Abdumalikov Jr., S. Berger, A. Wallraff, and S. Filipp. Microwave-controlled generation of shaped single photons in circuit quantum electrodynamics. *Phys. Rev. X*, 4:041010, 2014.

[34] Frank Pobell. *Matter and Methods at Low Temperatures*. Springer, 3rd edition,, 2006.

[35] David M. Pozar. *Microwave engineering*. John Wiley & Sons, Inc., 4th ed. edition, 2011.

[36] Jung-Tsung Shen and Shanhui Fan. Theory of single-photon transport in a single-mode waveguide. i. coupling to a cavity containing a two-level atom. *Phys. Rev. A*, 79(2):023837, 2009.

[37] Jung-Tsung Shen and Shanhui Fan. Theory of single-photon transport in a single-mode waveguide. ii. coupling to a whispering-gallery resonator containing a two-level atom. *Phys. Rev. A*, 79(2):023838, 2009.

[38] Mika A. Sillanpää, Jian Li, Katarina Cicak, Fabio Altomare, Jae I. Park, Raymond W. Simmonds, G. S. Paraoanu, and Pertti J. Hakonen. Autler-Townes effect in a superconducting three-level system. *Phys. Rev. Lett.*, 103(19):193601, Nov 2009.

[39] R. J. Thompson, G. Rempe, and H. J. Kimble. Observation of normal-mode splitting for an atom in an optical cavity. *Phys. Rev. Lett.*, 68(8):1132–1135, Feb 1992.

[40] M. Tinkham. *Introduction to Superconductivity*. McGraw-Hill International Editions, 1996.

[41] A.F. van Loo, A. Fedorov, K. Lalumière, B.C. Sanders, A. Blais, and A. Wallraff. Photon-mediated interactions between distant artificial atoms. *Science*, 342(6165):1494–1496, 12 2013.

[42] Arjan F van Loo. *Interactions in waveguide quantum electrodynamics*. PhD thesis, ETH Zurich, 07 2014.

[43] A. Wallraff, D. I. Schuster, A. Blais, L. Frunzio, R.-S. Huang, J. Majer, S. Kumar, S. M. Girvin, and R. J. Schoelkopf. Strong coupling of a single photon to a superconducting qubit using circuit quantum electrodynamics. *Nature*, 431:162–167, 2004.

[44] Huaixiu Zheng and Harold U. Baranger. Persistent quantum beats and long-distance entanglement from waveguide-mediated interactions. *Phys. Rev. Lett.*, 110:113601, Mar 2013.

Eidgenössische Technische Hochschule Zürich
Swiss Federal Institute of Technology Zurich

Declaration of originality

The signed declaration of originality is a component of every semester paper, Bachelor's thesis, Master's thesis and any other degree paper undertaken during the course of studies, including the respective electronic versions.

Lecturers may also require a declaration of originality for other written papers compiled for their courses.

I hereby confirm that I am the sole author of the written work here enclosed and that I have compiled it in my own words. Parts excepted are corrections of form and content by the supervisor.

Title of work (in block letters):

Nonclassical Light in waveguide QED:
Amplitude and Intensity Correlations

Authored by (in block letters):
For papers written by groups the names of all authors are required.

Name(s):	**First name(s):**
Mitchell	Bradley

With my signature I confirm that

- I have committed none of the forms of plagiarism described in the 'Citation etiquette' information sheet.
- I have documented all methods, data and processes truthfully.
- I have not manipulated any data.
- I have mentioned all persons who were significant facilitators of the work.

I am aware that the work may be screened electronically for plagiarism.

Place, date	**Signature(s)**
Zürich, 18 May, 2016	Brad Mitchell

For papers written by groups the names of all authors are required. Their signatures collectively guarantee the entire content of the written paper.